International Journal of Mechanical Sciences 195 (2021) 106263

Contents lists available at ScienceDirect

International Journal of Mechanical Sciences

journal homepage: www.elsevier.com/locate/ijmecsci

Fluid-structure interaction effects during the dynamic response of clamped thin steel plates exposed to blast loading

Vegard Aune[a,b,*], Georgios Valsamos[c], Folco Casadei[c], Magnus Langseth[a,b], Tore Børvik[a,b]

[a] Structural Impact Laboratory (SIMLab), Department of Structural Engineering, NTNU - Norwegian University of Science and Technology, Trondheim, Norway
[b] Centre for Advanced Structural Analysis (CASA), NTNU, Trondheim, Norway
[c] European Commission, Joint Research Centre (JRC), Ispra (VA), Italy

ARTICLE INFO

Keywords:
Lightweight structures
Blast mitigation
Shock tube
Numerical simulations
EUROPLEXUS

ABSTRACT

This work presents results from a numerical investigation on the influence of fluid-structure interaction (FSI) on the dynamic response of thin steel plates subjected to blast loading. The loading was generated by a shock tube test facility designed to expose structures to blast-like loading conditions. The steel plates had an exposed area of 0.3 m × 0.3 m and experienced large deformations during the tests. Numerical simulations were performed using the finite element code EUROPLEXUS. An uncoupled FSI approach was compared to a coupled FSI approach in an attempt to investigate FSI effects. Reduced deformation was observed in the plates due to the occurrence of FSI during the dynamic response. The general trend was an increased FSI effect with increasing blast intensity. The numerical results were finally compared to the experimental data to validate their reliability in terms of deflections and velocities in the steel plates. A good agreement with the experimental data was found, and the numerical simulations were able to predict both the dynamic response of the plate and the pressure distribution in front of the plate with good accuracy. Hence, the numerical framework presented herein could be used to obtain more insight regarding the underlying physics observed in the experiments. The clear conclusion from this study is that FSI can be utilized to mitigate the blast load acting on a flexible, ductile plated structure, resulting in reduced deformations.

1. Introduction

Civil engineering structures extend the scope of traditional blast-resistant design by also including architectural, lightweight and flexible structures [1–4]. These types of structures may experience severe blast-structure interaction between the propagating blast wave and the structural response (see, e.g., [5–9]). To meet the challenges posed by such extreme loading conditions, it is necessary to fully understand the importance of these interactions in view of blast-resistant design. Blast-structure interaction occurs when the blast wave encounters a structural surface that is not parallel to the direction of the wave. The blast wave is then reflected and reinforced. Depending on the blast and structural properties, the structure typically behaves as either a rigid or deformable surface. Fluid-structure interaction (FSI) takes place if the structural surface is allowed to move or deform.

Taylor [10] is considered to be one of the pioneers in the field of FSI in blast environments, suggesting that lightweight structures undertake less momentum compared to heavier structures when exposed to the same blast intensity. That is, the motion of the reflecting surface reduces the pressure acting on it. Recent years have seen a significant increase in the amount of research investigating the influence of FSI effects on the response of blast-loaded plates. Most of these studies have focused on plated structures in underwater blast environments [11–15]. These investigations typically assumed an acoustic medium characterized by an incompressible fluid and linear superposition of weak shock waves. Although the need to account for a compressible fluid behaviour was recognized [8,12,16,17], this was not taken into account during FSI in airblast environments until the works of Kambouchev et al. [6], Kambouchev [18], Kambouchev et al. [19,20], Vaziri and Hutchinson [21] and Hutchinson [22]. The acoustic assumption holds for underwater explosions, but compressibility effects are significant in air even for small magnitudes of blast overpressures. The compressible behaviour of air results in a significant increase in the magnitude of the stagnation pressure experienced by the structure during the blast-structure interaction since the reflected overpressure increases with the incident pressure in a highly non-linear manner. A basic understanding of the influence

* Corresponding author at: Structural Impact Laboratory (SIMLab), Department of Structural Engineering, NTNU - Norwegian University of Science and Technology, Trondheim, Norway.
E-mail address: vegard.aune@ntnu.no (V. Aune).

https://doi.org/10.1016/j.ijmecsci.2020.106263
Received 12 August 2020; Received in revised form 17 December 2020; Accepted 27 December 2020
Available online 4 January 2021

of FSI when the blast wave (in a compressible fluid) interacts with a movable or deformable surface is given in the works of Courant and Friedrichs [23], Toro [24] and Subramaniam et al. [25]. If the structure starts to move, the motion alters the pressure at its surface. Previous research has shown that FSI effects can mitigate the blast load acting on the structure [19–21,26], especially in situations involving large deformations [6,7,25,27]. The blast mitigation has been related to both the induced velocity [7,25] and to the deformed shape of the structure [26,28,29]. This is interesting in view of lightweight and flexible structures. Lightweight structures will experience a higher induced velocity and a reduction in the transmitted impulse after impact of the blast wave, while flexible structures will experience large inelastic deformation (see Ref. [30,31]) and a possible interaction of the dynamic response with the positive phase of the load. This implies that large deformations and energy absorption in structural members are favourable since the blast wave is mitigated through various deformation mechanisms in the structure. As long as the structural member can sustain the deformation that arises without experiencing failure, ductile materials can be utilized in the design of flexible structures by allowing for finite deformations. The FSI may then reduce the transmitted impulse and increase the blast performance of the structure. However, exploiting this mitigation effect in the blast-resistant design requires a thorough understanding of the governing physics in the problem.

Although approximate methods may provide design guidance, these methods are often based on several assumptions regarding the spatial and temporal distribution of the loading. Advanced numerical techniques are therefore often required for a sufficient insight in both the loading and the resulting dynamic response. A widely used design tool for this class of problems is the explicit non-linear finite element (FE) method [32]. The uncoupled approach is often the preferred procedure in today's blast-resistant design. The loading is then obtained using either empirical relations from the literature or numerical simulations of the blast wave propagation in an Eulerian (fixed) reference frame. The underlying assumption in this approach is rigid boundary conditions and no deformation of the structure, where the numerical simulations are typically performed in a computational fluid dynamics (CFD) code. These types of codes compute the fluid flow and provide the spatial and temporal pressure distribution along the fluid boundary. Then, the obtained pressure history is applied in a computational structural dynamics (CSD) code to determine the corresponding dynamic response of the structure. The uncoupled approach therefore makes the inherent assumption that the blast properties are unaltered by the structural motion and vice versa. Since the behaviour of blast-loaded steel plates is highly non-linear (both in the geometry and in the material), this may not be an adequate approach and could result in a non-physical response. Both the pressure distribution and the dynamic response can be significantly influenced by FSI effects. This was illustrated by Casadei et al. [5] and Børvik et al. [7] by comparing uncoupled and fully coupled FSI simulations for typical industrial applications. Børvik et al. [7] observed considerable variations in the predicted results from uncoupled and coupled methods and emphasized the importance of an accurate quantification of the loading. Recent advancements [33,34] in the field of FE methods make it now possible to study the FSI effects in blast events involving complex geometries, large deformations, failure and fragmentation. In particular, adaptive mesh refinement (AMR) [35–38] in both the fluid (F) and structural (S) sub-domains allows for a sufficiently fine mesh size to represent the near instantaneous rise in pressure across the shock wave and to predict the pressure distributions at the F-S interface. Numerical simulations can therefore be used to investigate the effect of FSI on the dynamic response of plated structures. However, before such methods can be used, it is essential to evaluate their performance in terms of robustness, reliability and effectiveness in predicting both the loading and the dynamic response. Experimental validation is often preferred as it represents the actual physics in the problem, and controlled experiments in laboratory environments can be used to evaluate current computational methods.

This motivates detailed investigations on FSI effects during the dynamic response of blast-loaded steel plates. Previous studies [36,39–41] were not able to fully address FSI effects during the dynamic response of the plates, mainly because the loading was significantly overestimated in the numerical simulations at increasing magnitudes of pressure. The current work has managed to considerably improve the predictive capabilities of the simulations, allowing for detailed studies on the underlying physics during FSI. Therefore, the objectives of this study are as follows: (1) establish a reliable numerical methodology based on recent developments in EPX; (2) numerically quantify the influence of FSI effects on the dynamic response of thin steel plates; and (3) use existing experimental data [36] to evaluate the performance of the numerical simulations and ensure that the underlying physics are captured.

2. Experimental work

Experiments were performed in the SIMLab Shock Tube Facility (SSTF) at NTNU. A detailed presentation of the design, evaluation of its performance and the experimental programme used herein can be found in Refs. [36,39]. However, the experimental setup and programme are briefly repeated in the following for completeness since most of these tests served as the basis for the final evaluation of the numerical simulations that will be presented in Section 4. The SSTF has been proven to produce controlled and repeatable blast loading in laboratory environments [39], and it is considered to be well suited to study FSI effects during the dynamic response of blast-loaded plates (see, e.g., [36,39–41]).

The overall principle is that of a compressed-gas-driven shock tube, in which a high-pressure chamber (called driver in Fig. 1a) is separated from a low-pressure chamber (called driven in Fig. 1a) by using multiple diaphragms. A sudden opening of the diaphragms generates a shock wave travelling down the tube and into the low-pressure chamber. By using a relatively small ratio between the lengths of the high-pressure and low-pressure chambers, this experimental setup differs from traditional shock tubes in the way that the reflected rarefaction waves catch up with the shock wave resulting in pressure profiles similar to the blast wave from an explosive detonation [39,42].

The total length of the tube is 18.355 m and it is made from stainless steel of grade P355NH, which is intended for pressure purposes according to the EN 13445. The high-pressure chamber (called driver in Fig. 1a) is manufactured with a total length of 2.02 m and has a circular cross-section with an inner diameter of 0.331 m, where the internal wall is dull polished to obtain a smooth surface. Aluminium inserts may be used to reduce the effective length of the driver section in 0.25 m increments. The driver is followed by a 0.14-m-long firing section that consists of several intermediate pressure chambers separated by diaphragms (Fig. 1a and 1c). This enables the total pressure difference between the driver and driven section to be achieved in a stepwise manner. The test starts by filling the driver and firing section with compressed air, where the pressure differences in the intermediate chambers are operated below the diaphragm rupture strength such that the desired pressure is obtained in the driver. Rupture of the diaphragms is initiated by controlled and rapid venting of the intermediate pressure closest to the driver section using two solenoid valves. This ensures a controlled rupture of the diaphragms and reproducible bursting pressures. The bursting pressure may be varied by changing the thickness of the diaphragms. Melinex sheets are used as diaphragms due to this material's strength and repeatability.

The inner cross-section in the driven section starts with a 0.6-m-long transition region from circular to square cross-section (at constant area), where the square cross-section continues until the very end of the tube (Fig. 1a). An epoxy material is used to obtain a smooth surface and a square cross-section of 0.3 m × 0.3 m inside the surrounding tube (Fig. 1d). The epoxy material works as a practically incompressible material, while the surrounding tube ensures the structural strength. The

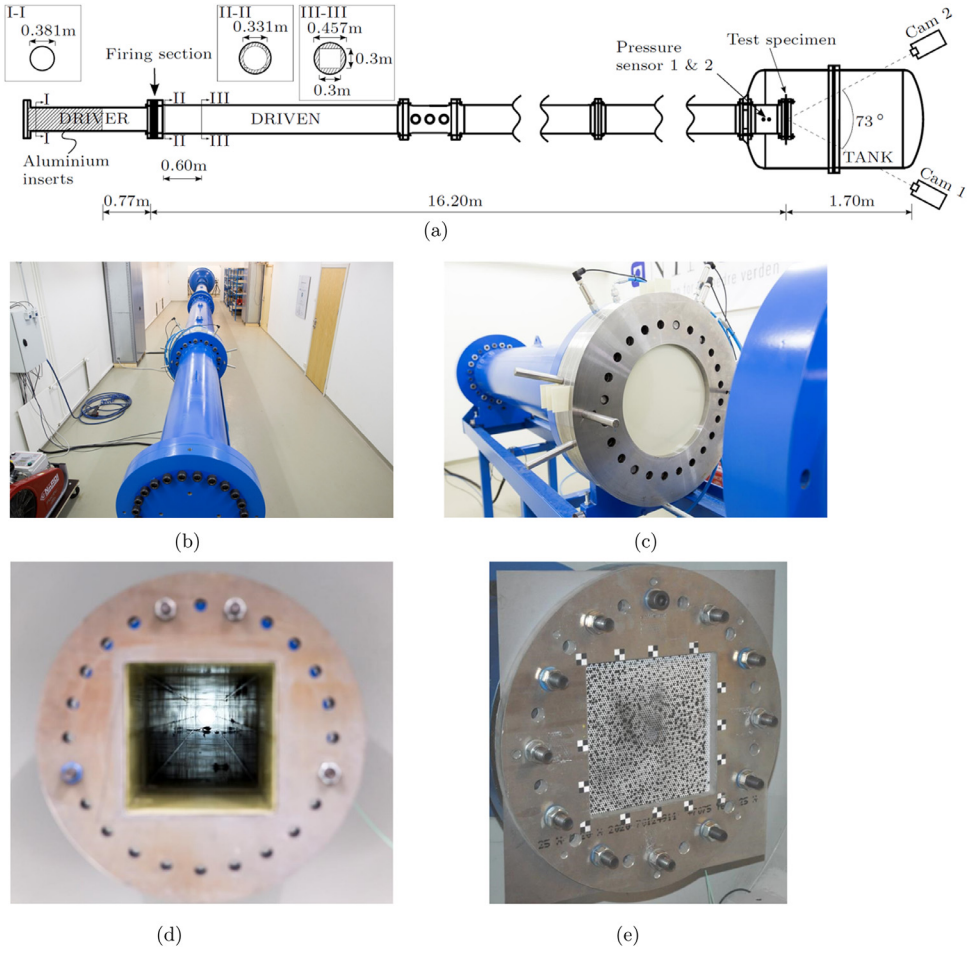

Fig. 1. Experimental setup of the SIMLab Shock Tube Facility (SSTF): (a) Sketch of the experimental setup (seen from above), picture of the (b) shock tube (seen from the driver section), (c) firing section (seen from the driven section), (d) internal cross-section of the driven section (seen from the cameras) and (e) clamping and DIC speckle pattern for the flexible steel plate (seen from the cameras). Reprint from Aune et al. [36,39], Aune [41].

Table 1
Test matrix including initial conditions and representative blast properties for each test.

Test	Initial conditions			Blast properties*			
	Pressure (driver) [kPa]	Pressure (driven) [kPa]	Temperature [°C]	M_s [-]	$p_{r,max}$ [kPa]	i_{d+} [ms]	i_{r+} [kPa ms]
D05	637.6	100.5	21.9	1.37	267.5	28.7	2557.9
D15	1716.0	100.8	21.4	1.63	606.6	44.1	7510.0
D25	2811.0	100.8	21.0	1.75	795.2	68.7	12,383.3
D35	3914.0	100.7	22.2	1.88	1105.2	73.9	16,613.4
D60	6307.0	100.6	23.0	2.04	1446.1	75.3	21,151.7

*Representative blast properties obtained from massive, non-deformable plates in Ref. [39] from tests with similar initial conditions.

average roughness (Ra) of the surfaces inside the driven section is reported by the manufacturer to be in the range of 0.2–0.4 μm.

In the present work, the length of the driver and driven sections was 0.77 m and 16.20 m (Fig. 1a), respectively, both with a cross-sectional area of 0.09 m^2. The blast intensity was varied by changing the initial pressure in the driver section, while the initial pressure in the driven section was at ambient conditions. Table 1 gives the test matrix used herein, where each test is numbered DY in which D denotes deformable steel plate (D) and Y indicates the firing (absolute) pressure in bars in the driver. From Table 1, it is noted that the test numbers are rounded to the lower multiple of 5 for the firing overpressures (in bars). A thin Docol 600DL steel plate was mounted at the end of the tube to introduce moving boundary conditions (Fig. 1e). The deformable steel plates with dimensions 0.625 m × 0.625 m × 0.0008 m were clamped to the end flange of the tube in an attempt to achieve fixed boundary conditions (Fig. 1e). Each of the 12 bolts was tightened using a wrench with a torque M_t of 200 Nm. This is equivalent to a pre-tensioning force F_p of 46.6 kN for the M24 bolts used in the SSTF [36]. The plates had an exposed area of 0.3 m × 0.3 m (equal to the internal cross-section of the tube).

To establish a basis for comparison of the dynamic response in the numerical simulations, the steel plates were spray-painted with a speckle pattern (Fig. 1e) and three-dimensional digital image correlation (3D-DIC) analyses were carried out to measure the transient displacement field. The stereovision setup of the two high-speed cameras (Phantom v2511) is illustrated in Fig. 1a. The 3D-DIC was performed using the in-house DIC code eCorr [43] comparing the greyscale-value field of the speckle pattern for an image in the deformed (current) configuration to that in the undeformed (reference) configuration.

Piezoelectric pressure sensors (Kistler 603B) were used to measure the pressure 24.5 cm (Sensor 1) and 34.5 cm (Sensor 2) upstream of the test specimen (Fig. 1a). The pressure sensors were flush mounted in the

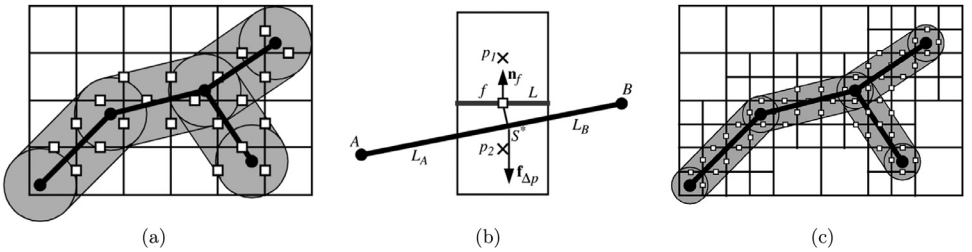

Fig. 2. Weak coupling using CCFVs in the embedded FSI approach: (a) faces in the influence domain, (b) calculation of the pressure drop force $\mathbf{f}_{\Delta p} = (p_1 - p_2)L\mathbf{n}_f$ and (c) improving algorithm spatial resolution by FSI-driven AMR in the fluid (only one refinement level shown for simplicity). (a) and (b) are reprints from Casadei et al. [34].

roof of the shock tube, automatically triggered when the shock wave arrived at Sensor 2 and operated with a sampling frequency of 500 kHz. The pressure measurements were also synchronized with the high-speed cameras operating at a recording rate of 24 kHz. The dynamic response in terms of mid-point deflections and the pressure measurements at Sensor 1 in tests D05 to D35 were already reported in Ref. [36]. The experimental results will be presented and used for validation of the numerical simulations in Section 4.

The blast intensity is typically represented as a pressure history $p(t)$ described by the peak reflected overpressure $p_{r,max}$, the duration of the positive phase t_{d+} and the positive specific impulse i_{r+}. The Mach number M_s is also frequently used to indicate the blast intensity. The representative blast properties obtained from massive, non-deformable plates in Ref. [39] from tests with similar initial conditions are also included in Table 1 for completeness.

3. Numerical study

The numerical simulations were performed by the explicit FE code EUROPLEXUS (EPX) [44], which is jointly developed by the French Commissariat à l'Energie Atomique et aux Energies Alternatives (CEA) and by the Joint Research Centre of the European Commission (JRC). The Cast3M software [45], also developed by CEA, was used to generate the FE meshes for the various numerical models, while the ParaView software [46] and EPX itself were used for post-processing of the numerical results. In the fully coupled FSI simulations presented in this study, both the fluid sub-domain and the structural sub-domain are included to be able to study the influence of FSI effects on the dynamic response of blast-loaded steel plates. A detailed presentation of the governing equations for the structural and fluid sub-domains can be found in the Appendix.

3.1. Modelling of FSI

The fluid sub-domain was discretized with cell-centred finite volumes (CCFV) because they are superior to traditional finite elements (FE) regarding modelling of discontinuities in the fluid flow. Coupling between the structural sub-domain and the fluid sub-domain is achieved by an FSI algorithm of the embedded (or immersed) type, known as *FLSW* in EPX; see Ref. [34] and Fig. 2. This particular algorithm is chosen among various others present in EPX for two main reasons. The first reason is the use of CCFV in the fluid sub-domain, and the second reason is the possibility for the test specimen to undergo large rotations and large deformation.

The structure and the fluid are meshed independently, and then, the structural mesh is simply embedded into (i.e., superposed to) the fluid mesh, as shown in Fig. 2a. This dramatically simplifies preparation of the numerical model compared with other (mesh-conforming) FSI techniques, but it requires more CPU-intensive calculations and may slightly reduce the accuracy of the results for a given size of the mesh. However, this technique is most favourable in the case of large deformations of the structure, see Ref. [34].

The *FLSW* technique follows a so-called weak coupling based on direct application of fluid forces to the structure. The fluid forces arise from the fluid pressure computed at the CCFV centroids. *FLSW* is the most natural choice when using the embedded approach and CCFVs for the fluid sub-domain [33]. This is opposed to the so-called strong coupling of other FSI techniques based upon constraints (via Lagrange multipliers) on the velocities at the fluid nodes, which is the preferred approach when FEs are used for the fluid. *FLSW* operates on the numerical fluxes of mass and energy at CCFV interfaces interacting with the structure. These fluxes are blocked (Fig. 2b) in order to prevent spurious passage (leakage) of fluid across the structure, as long as the plate does not fail. This produces a sort of (weak) feedback on the fluid flow, due to the presence of the structure. The fluid forces are assembled with other potential external forces (see the Appendix and $\boldsymbol{F}^{ext}$ in Eq. (2)) and subsequently used to calculate the dynamic equilibrium of the structure.

With reference to Fig. 2, in order to determine the portions of fluid (thin regular mesh) interacting with the structure (thick solid lines), the so-called structural influence domain is considered (grey zone). Each CCFV interface (small hollow square) located inside the influence domain transmits a load to the nearest point of the structure proportional to the pressure drop between the two fluid cells forming the interface. A crucial part of the algorithm is the fast update of the structural influence domain and the fast search for the interacting fluid entities (CCFV interfaces in this case) at each time step of the numerical simulation. Recent advancements [35–38,40] in EPX allow for automatic adaptive mesh refinement (AMR) near the fluid-structure interface (FSI-driven adaptation of fluid mesh), which improves the accuracy of the embedded approach. As shown in Fig. 2c (with just one level of adaptive refinement for simplicity), by reducing the size of the fluid cells close to the structure, the thickness of the structural influence domain can be reduced accordingly, thus increasing the accuracy of the embedded FSI algorithm.

3.2. Numerical models

A fully coupled FSI model using one quarter of the experimental setup (by exploiting longitudinal symmetries) was established (see Fig. 3c). The steel plate and diaphragms were modelled using a Lagrangian discretization with Reissner-Mindlin shell elements (quadrangles *Q4GS* and triangles *T3GS*). A mesh convergence study showed that a mesh size of 10 mm was adequate to reproduce the observed global deformation. The steel plate and diaphragms were therefore modelled with an element size of approximately 6 mm and 10 mm, respectively, as the base mesh prior to adaptive refinement (where AMR was applied to the diaphragms). The diaphragms were modelled using only *Q4GS* elements, while the steel plate was represented using both *Q4GS* and *T3GS*. *Q4GS* is a 4-node element with 6 dofs per node and 20 integration points (4 in the plane, 5 through the thickness), and *T3GS* is a 3-node element with 5 integration points (1 in the plane, 5 through the thickness). Simplified boundary conditions were used for the diaphragms, while the steel plate included the complete clamping assembly. Thus, only the exposed area of the diaphragms was modelled and all the nodes located along the perimeter were fully fixed against translation in all directions (Fig. 3a). The importance of including the diaphragm failure process in the simulation of blast wave propagation in shock tubes was illustrated by Andreotti et al. [47]. It was found that the diaphragm failure

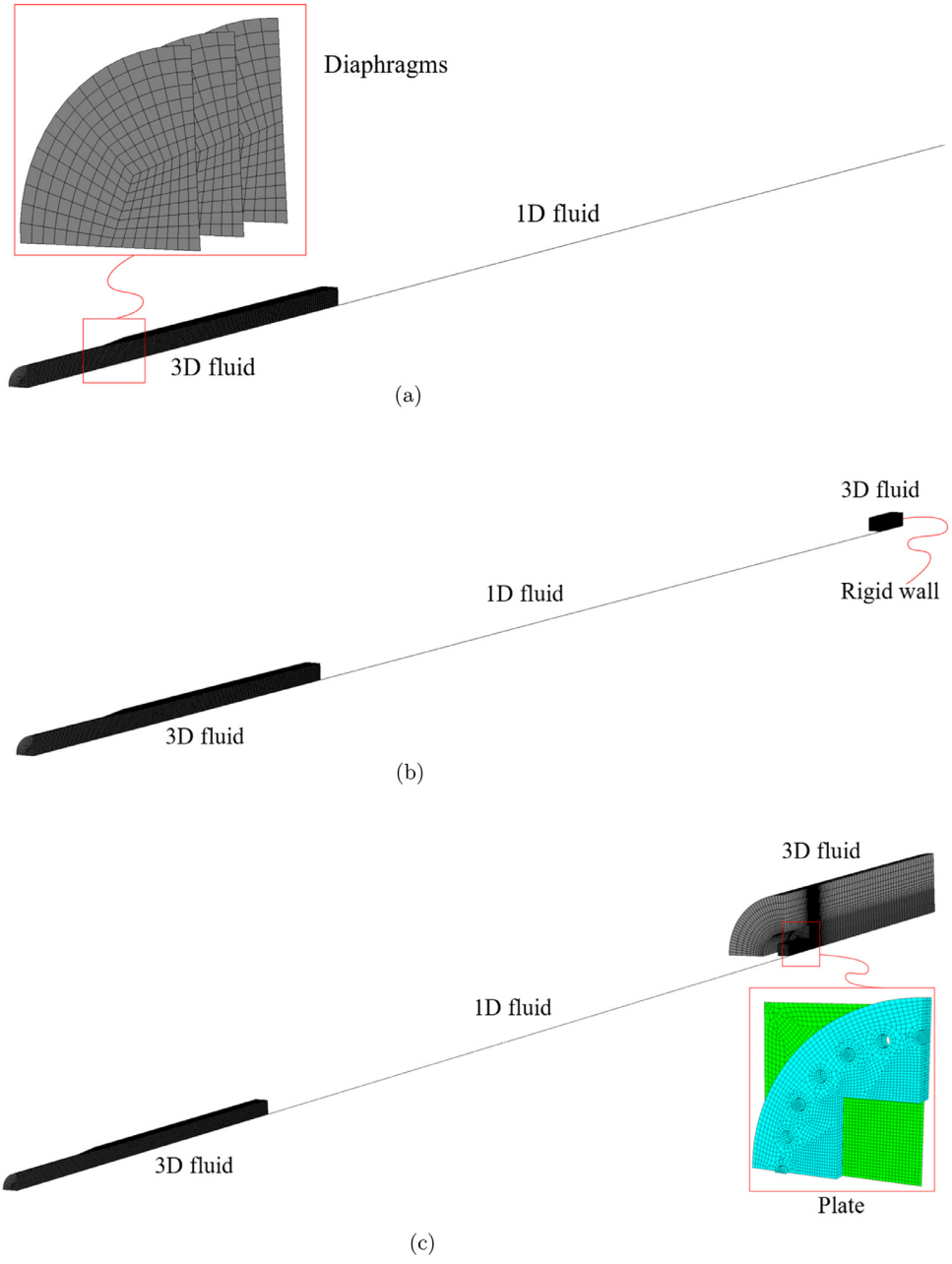

Fig. 3. Numerical model (1/4) of the (a) mapping simulation, (b) fluid sub-domain in the first part of the uncoupled approach (see case B2 in Fig. 4) and (c) fully coupled FSI approach. The plate assembly shown in (c) was also used (stand-alone) in the second part of the uncoupled approach.

process introduces a multi-dimensional flow field downstream of the diaphragms, which was observed as a loss of directional energy in the distant flow field. The diaphragm failure process will therefore affect the reflected overpressure on the steel plates located at the rear end of the tube.

The fluid sub-domain was partly discretized by 1D finite volumes (segments of *TUVF*) and partly by 3D finite volumes (bricks of *CUVF*); see Fig. 3. An initial mesh size of 10 mm was used in the entire 1D-domain, in the first part of the 3D-domain and in the vicinity of the plate, according to the mesh sensitivity study in Ref. [39,41]. The cell size in the tank was increased up to 80 mm towards the internal walls. This resulted in 1210 *TUVF*s and 190,527 base *CUVF*s in the fluid sub-domain before AMR application (where appropriate). The motivation for using *TUVF*s in-between the two regions with *CUVF*s was twofold: to reduce the CPU cost by reducing the number of finite volumes and to enable the use of the *PARO* directive in EPX [44]. The *PARO* directive allows accounting for friction and heat exchange against the interior walls of the tube by specifying the average roughness (0.4 micrometres).

The 3D mesh of the fluid sub-domain starts with a circular cross-section in the driver and firing sections. Then, a transition part of 0.6 m length follows immediately downstream the diaphragms, which starts with the circular cross-section in the driver and ends with the square cross-section in the driven section throughout the following 3.3 m of the shock tube (see Fig. 3). This 3D part of the mesh is then followed by a 1D part until reaching 0.6 m upstream of the test specimen, with suitable couplings between the 1D and 3D parts of the fluid mesh (*TUBM* junction elements). That is, the *TUBM* connects the 1D part of the fluid using *TUVF*s to the faces of the neighbouring *CUVF*s in the 3D part of the fluid. It is emphasized that the location of the junction element should coincide with a uniform fluid field at this point in the model. The fluid sub-domain considers the computational mesh fixed (Eulerian formulation), while the fluid (particles) moves relative to these grid points. CCFVs were used, and the numerical fluxes between adjacent CCFVs were cal-

culated using the approximate Harten-Lax-van-Leer-Contact (HLLC) Riemann solver [24,44], where stability in the convection phase of the explicit solution in time was ensured by using a Courant-Friedrichs-Lewy (CFL) coefficient of 0.4. CCFVs have an inherent rigid-wall boundary condition due to the integral form of the governing equations, where the flux at the cell boundary is blocked if there is no neighbouring cell. Thus, there is no need to explicitly impose any boundary conditions on the CCFVs adjacent to the shock tube walls. The HLLC solver was chosen due to its favourable characteristics with respect to limiting the numerical diffusion when computing the fluxes at the interfaces of the CCFVs. The Van Leer-Hancock predictor-corrector scheme was utilized in the CCFV to achieve second-order accuracy in time. Second order in space was reached via the Green-Gauss reconstruction of the conservative variables using a Dubois limiter to mitigate the possibility of numerical instabilities at the shock front where the solution is discontinuous. The resulting numerical scheme is total variation diminishing (TVD). A sensitivity study was carried out to evaluate the influence of the Dubois limiter coefficient [44], a number between 0 and 1, with higher values corresponding to more accurate but also potentially unstable results. It was found that the default value used in EPX (0.50) gave equally good results as other more aggressive values (0.75).

Based on the information from the manufacturer, the Melinex diaphragms were assumed to behave elasto-plastically until fracture. Depending on the thickness of the diaphragms, the yield stress and plastic modulus were in the range of 100–160 MPa and 13.9–54.7 MPa, respectively. Fracture was modelled using element erosion and was initiated when all the integration points in the respective element reached a critical value of 100 % for the maximum principle strain. In an attempt to predict the crack propagation observed in the experiments, use was made of AMR of the diaphragms driven by the accumulated plastic strain p. Recent advancements [35] in EPX allow for AMR based on user-defined criteria, which makes it convenient to relate the AMR to the plastic strain. That is, the mesh refinement occurs at user-defined levels of the plastic strain and at successive levels of refinement. This study used up to two successive refinements within the range of $0.01 \leq p \leq 0.4$, resulting in a minimum element size of 2.5 mm when $p > 0.4$. Ductile fracture of the diaphragms could then be predicted without too much loss of mass when using element erosion in combination with AMR.

The diaphragms are completely decoupled from the fluid during the filling process. That is, the diaphragms are first loaded by an externally imposed pressure similar to that of the compressed air in the driver (see Table 1). Once equilibrium is reached around the deformed configuration, the externally imposed pressure is removed and the fluid states are initialized in the driver, firing and driven chambers. The pressure gradients over the diaphragms will then ensure equilibrium until rapid venting of the firing section initiates the diaphragm fracture process. An embedded FSI technique (*FLSW*) [34,44] and FSI-driven AMR was used for the coupling at the fluid-diaphragm (F-D) interface. FSI-driven AMR was activated in the fluid sub-domain to obtain a sufficiently refined fluid mesh at the F-D interface.

The *FLSW* FSI technique and FSI-driven AMR were also used in the fluid for the coupling at the fluid-structure (F-S) interface between the fluid and the steel plate. EPX then enables automatic refinement of the fluid mesh in the vicinity of the plate that can move and undergo large deformations. This allows for a sufficiently fine fluid mesh size to represent the near instantaneous rise in pressure over the blast wave. A mesh sensitivity study showed that a mesh size of 5 mm was sufficient to capture the governing physics in the fluid sub-domain. The number of AMR-generated elements was approximately 300,000 *CUVF* in the fluid at the F-D interface, 10,000 *Q4GS* in the diaphragms and 200,000 *CUVF* in the fluid at the F-S interface. Contact is activated between the various diaphragms and between the diaphragms and tube walls to avoid inter-penetration during the diaphragm failure process.

The symmetry of the model was also exploited when modelling the plate and clamping assembly using a 1/4 model with suitable geometry constraints (see Fig. 3c). The bolts and the clamping frames were represented by solid elements with 3 dofs per node using both the 8-node brick element *CUB8* with 8 integration points and the 6-node wedge element *PR6* with 6 integration points. Material parameters for the steel clamping frames were taken from Ref. [36] using the *VPJC* model (see the Appendix, Eq. (7) and Table A.1). Each of the bolts was pre-stressed to an initial torque ($M_t = 200$ Nm), resulting in a clamping pressure between the frames and the plate. This was accounted for by modelling the lower clamping frame and bolts as one initially stress-free component, while an external pressure was applied at the contact area between the bolt head and the upper clamping frame. The contact pressure was determined using the approach suggested in Ref. [36], resulting in a contact pressure of 44 MPa applied over the contact area for each nut (1060 mm^2) throughout the simulation. The clamping pressure was imposed via 4-node boundary condition elements *CL3D*. These elements automatically recognize the solid elements to which they are attached and use the assigned pressure histories. The lower clamping frame was fully blocked at its back surface.

Contact between the plate, bolts and frames was modelled using a node-to-surface contact algorithm (*GLIS*) utilizing slave nodes and master surfaces where contact was enforced by Lagrangian multipliers when a slave node penetrated a master surface. The plate was modelled as the slave, and both the static and the dynamic friction coefficient between the plate and clamping frames were set to 0.50, a typical value from the literature for a steel-to-steel interface. A detailed presentation of the numerical modelling of the steel plate and clamping assembly is found in Aune et al. [36]. It should be emphasized that the modelling of the clamping assembly was essential to obtain accurate plate deformation. This is because the plate slides somewhat between the clamping frames while deforming. Thus, the plate cannot be simply considered as fixed along the perimeter of the exposed area, since this would result in an overly constrained behaviour of the plate.

3.3. Computational methodology to study FSI effects

Fluid-structure interaction (FSI) effects are studied by comparing the numerical predictions of the uncoupled and coupled FSI approaches. A schematic representation of the computational framework adopted in the present work is presented in Fig. 4. That is, prior to the simulations using either the uncoupled or the coupled approach, a preliminary simulation was performed using the numerical model presented in Fig. 3a, including the detailed representation of the diaphragm failure process and its influence on the blast wave formation along the shock tube in each of the tests (see textbox A in Fig. 4). This simulation generates a so-called map file containing, for each fluid finite volume, the physical conditions just before the shock wave reaches the right end of the 1D fluid sub-domain. The mapping procedure was possible since all the numerical models presented in Fig. 3 used the exact same fluid discretization throughout the first 3D and 1D parts of the mesh. Fig. 5 shows the diaphragm failure process in the preliminary simulation of test D35. Both FSI-driven AMR (in the fluid) and plasticity-based AMR (in the diaphragms) are used for a detailed representation of the diaphragm rupture and its influence on the flow field.

Then, an uncoupled simulation approach is performed consisting of two steps (see textbox B in Fig. 4). The first step (B1) is an Eulerian (fluid-only) simulation using the map file as initial conditions in the fluid sub-domain and producing the pressure time history $p(t)$ on the rigid wall (plate location) in Fig. 3b. Thus, the uncoupled simulations make the inherent assumption that the pressure is unaltered by the structural motion, and vice versa. The uncoupled approach is therefore a conservative simplification of the real behaviour because it is expected that this approach will overestimate the actual pressure since the plate is not allowed to deform in the Eulerian simulations. The uncoupled approach will therefore be used in the following as a reference to identify FSI effects during the dynamic response of the deformable plates. The reflected overpressures obtained on the rigid wall in the Eulerian

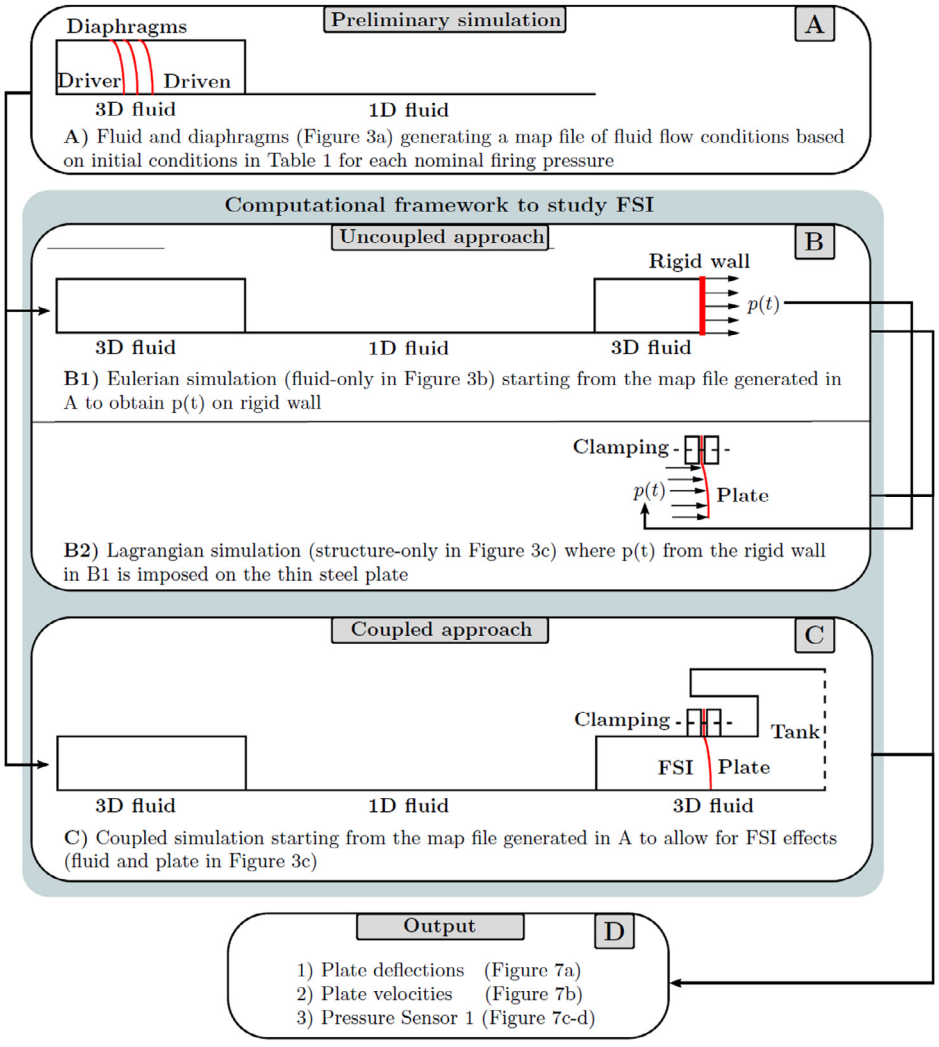

Fig. 4. Conceptual scheme of the strategy used to study FSI effects by using the numerical models in Fig. 3. Note that both the Eulerian simulations in the uncoupled approach and the FSI simulations in the coupled approach started from the same initial conditions in the fluid sub-domain (map file), ensuring that the incoming blast wave was identical in both approaches.

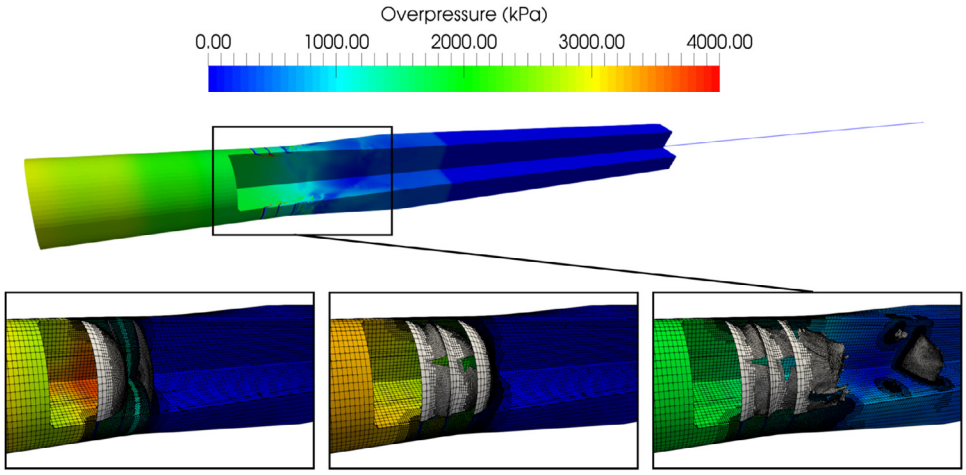

Fig. 5. Illustration of the preliminary simulation including the diaphragms failure process. Upper view provides the complete view of the pressure field for the entire model, while the lower view contains a close up on the diaphragms and the fluid in the vicinity of the diaphragms immediately before rupture (left), just after rupture (middle) and at complete failure (right). Note the automatic AMR acting both on the fluid (FSI-driven) and on the diaphragms (plastic-strain driven).

simulations are shown in Fig. 6. The second step (B2) of the uncoupled approach is a Lagrangian (structure-only) simulation including only the thin steel plate and the clamping assembly shown in the right part of Fig. 3c. This simulation uses the pressure history $p(t)$ predicted in the Eulerian simulation as an imposed loading to obtain the corresponding dynamic response of the plate. Analogous to the clamping pressure, the blast pressure on the exposed area of the plate was modelled by *CL3D* boundary condition elements. The blast pressure was imposed as a uniformly distributed pressure on the exposed area of the steel plate in the uncoupled approach. The uniform distribution was justified by the Eulerian simulation, which predicted a uniform blast pressure at the rigid wall.

Finally, a simulation following the coupled approach is carried out for each of the tests in Table 1, using the corresponding map file to

Table 2
Numerical results in terms of blast properties from the Eulerian simulations and pressure measurements $p_{r,max}$ and the corresponding saturated impulse $i_{r+,sat}$ at Sensor 1 in the uncoupled and coupled FSI approach. The FSI effects $\Delta p_{r,max}$ and $\Delta i_{r,+}$ are also given.

Test	Blast properties*				Pressure measurements at Sensor 1					
	Eulerian simulations				Uncoupled approach		Coupled approach		FSI effects**	
	M_s [-]	$p_{r,max}$ [kPa]	t_{d+} [ms]	i_{r+} [kPa ms]	$p_{r,max,u}$ [kPa]	$i_{r+,sat,u}$ [kPa ms]	$p_{r,max,c}$ [kPa]	$i_{r+,sat,c}$ [kPa ms]	$\Delta p_{r,max}$ [%]	$\Delta i_{r+,sat}$ [%]
D05	1.28	258.60	28.5	2659.0	242.0	280.8	231.5	257.9	-4.3	-8.1
D15	1.64	595.90	51.3	8633.3	552.0	503.2	500.3	448.1	-9.4	-11.0
D25	1.74	800.60	74.1	16,361.4	743.0	641.4	663.8	569.2	-10.7	-11.3
D35	1.84	1097.50	86.4	23,513.6	1045.2	876.7	916.5	747.5	-12.3	-14.7
D60	2.09	1462.00	89.0	36,951.5	1401.7	1091.9	1191.8	951.6	-15.0	-12.8

*Blast parameters representing the pressure histories at the rigid wall in Fig. 3b. **$\Delta p_{r,max} = (p_{r,max,c} - p_{r,max,u})/(p_{r,max,u}) \times 100\%$, $\Delta i_{r+,sat} = (i_{r+,sat,c} - i_{r+,sat,u})/(i_{r+,sat,u}) \times 100\%$.

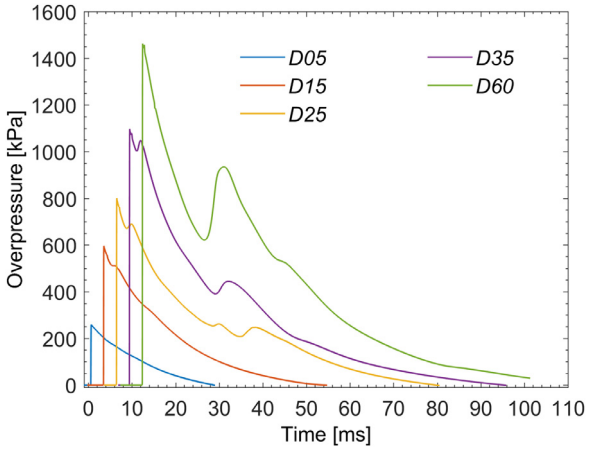

Fig. 6. Pressure curves obtained on the rigid wall in the Eulerian simulations (see Fig. 3b). These pressure histories are used to load the plates in the purely Lagrangian simulations (uncoupled approach). Note that the curves are shifted in time for improved readability. Each curve was right-shifted 3 ms with respect to the previous one.

Table 3
Numerical results from the uncoupled and coupled FSI approach in terms of mid-point deflections, saturated durations $t_{d+,sat}$ and the FSI effect $\Delta d_{z,max}$.

Test	Mid-point deflections and saturated time*						
	Uncoupled approach			Coupled approach			FSI effect**
	$d_{z,max,u}$ [mm]	$d_{z,p,u}$ [mm]	$t_{d+,sat,u}$ [ms]	$d_{z,max,c}$ [mm]	$d_{z,p,c}$ [mm]	$t_{d+,sat,c}$ [ms]	$\Delta d_{z,max}$ [%]
D05	16.5	13.6	1.26	15.8	12.9	1.21	-4.1
D15	26.9	25.3	0.97	24.9	23.1	0.94	-7.5
D25	32.9	31.3	0.92	29.7	28.2	0.89	-9.5
D35	41.0	39.7	0.88	36.3	34.9	0.84	-11.4
D60	50.4	49.2	0.82	43.4	42.2	0.79	-13.8

*$t_{d+,sat}$ = the time it takes from the start of plate movement until permanent deformation $d_{z,p}$. **$\Delta d_{z,max} = (d_{z,max,c} - d_{z,max,u})/(d_{z,max,u}) \times 100\%$.

set the initial conditions in the fluid sub-domain and including both the fluid and structural sub-domain in the same simulation (see textbox C in Fig. 4). It is important to emphasize that both the Eulerian simulation in the uncoupled approach and the FSI simulation in the coupled approach started from the same initial conditions in the fluid sub-domain (map file), ensuring that the incoming blast wave is identical in both approaches. This allows for numerical investigations on FSI effects during the dynamic response of the plates based on the output listed in textbox D. The results from the fully coupled simulations are therefore compared to the corresponding results obtained with the uncoupled FSI approach. Experimental results will finally be compared to the fully coupled simulations in Section 4 to ensure that the numerical predictions are reasonable.

3.4. Quantification of FSI effects

In blast-resistant design, the reflected overpressure is typically represented as a pressure history $p(t)$ described by the peak reflected overpressure $p_{r,max}$, the duration of the positive phase t_{d+} and the positive specific impulse i_{r+}. The Mach number M_s is also frequently used to indicate the blast intensity. These blast parameters are therefore listed in Table 2 for completeness in the evaluation of the blast properties in the shock tube tests. The blast parameters were obtained from the pressure histories on the rigid wall in the purely Eulerian simulations (see Fig. 6).

It is important to emphasize that these shock tube tests were found to be in the dynamic loading domain by Aune et al. [36]. This classification was based on the ratio between the positive phase duration t_{d+} and the natural period of vibration T_n in the plates. The natural period of vibration T_n was estimated to be 12.5 ms, resulting in ratios t_{d+}/T_n ranging from 2.3 to 7.1 for the tests listed in Table 2. Hence, it is not the total impulse i_{r+} of the loading that governs the dynamic response but rather the profile of the loading history due to the overlapping of the plate response with the positive phase duration t_{d+} (see, e.g., [48]). Therefore, in the dynamic loading domain, it is only the saturated part of the impulse $i_{r+,sat}$ that contributes to the plate deformation. Focusing on the total reflected impulse i_{r+} might be misleading since only the saturated impulse $i_{r+,sat}$ is responsible for the permanent deformation of the plates. This work adopts the definition of the saturated impulse $i_{r+,sat}$ as suggested in the work by Bai et al. [4], i.e., the reflected impulse until the saturated duration $t_{d+,sat}$ that corresponds to the time of permanent deformation $d_{z,p}$ in the plates. The saturated duration $t_{d+,sat}$ therefore corresponds to the period of time in which the plate experiences permanent deformations. Beyond this period, the motion of the plate ceases and the plate mainly undergoes minor elastic vibrations around its permanent deformed configuration. The saturation phenomenon will be further addressed when discussing the results presented in Fig. 7.

Fig. 7a-b compare the mid-point deflections and mid-point velocities (obtained by differentiating the deflections in time) in the plate, respectively, for the coupled approach to those in the uncoupled approach, while Fig. 7c contains the pressure histories at the computational cell (*CUVF*) closest to the point where Sensor 1 was located in the experiments. Maximum mid-point deflections $d_{z,max}$, permanent mid-point deflections $d_{z,p}$ and the saturated duration $t_{d+,sat}$ are summarized and compared to the uncoupled approach in Table 3. Negative values of the difference in maximum deflection $\Delta d_{z,max}$ imply that the maximum mid-point deflections are larger in the uncoupled approach. It should

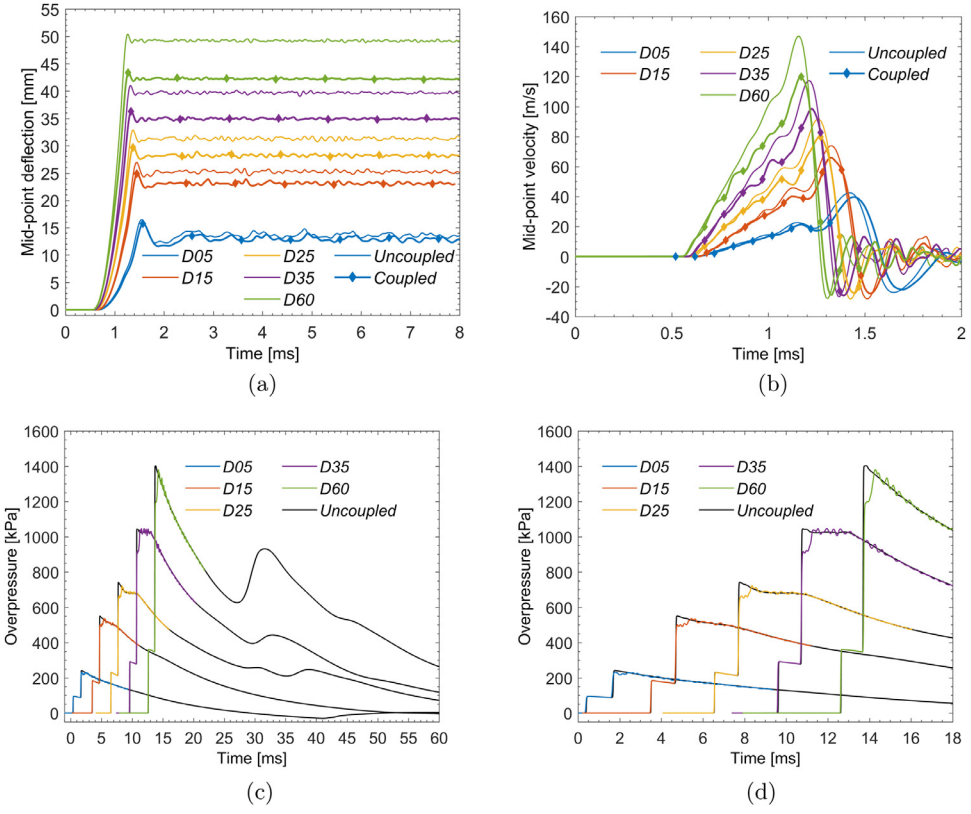

Fig. 7. Investigation of FSI effects on the (a) mid-point deflections, (b) the induced mid-point velocity in the plates, (c) pressures measured at Sensor 1 and (d) the same data as (c) where the time axis is more focused on the reflected overpressure. Note that the curves in (c) and (d) are shifted in time for improved readability. Each curve was right-shifted 3 ms with respect to the previous one.

be noted that Fig. 7d contains the same data as Fig. 7c; however, the time axis is more focused on the reflected overpressure at Sensor 1. The main purpose of Fig. 7d is therefore to illustrate the influence of FSI on the peak reflected overpressure. In addition, note that the simulations following the coupled approach were intentionally stopped earlier than the corresponding uncoupled simulations (see Fig. 7c). This was because, on the one hand, the dynamic response of interest was already reached at this point in time, while, on the other hand, the remaining part of the coupled simulation would require a significant CPU cost due to the decrease in the critical time step caused by the FSI-driven AMR in the fluid close to the plate.

As expected, the uncoupled approach predicts larger deformations than the corresponding fully coupled FSI simulation (Fig. 7a and Table 3). It is observed that the mid-point deflections are reduced by approximately 4-14 % when considering FSI. The clear trend is that higher pressure magnitudes result in increased FSI effects during the dynamic response of the plates. The same trend was observed for the induced velocities in the plates (Fig. 7b). Fig. 7c-d show a reduction in the initial peak reflected overpressure in the coupled simulations, where a slight trend of an increased reduction at increasing pressure magnitudes is observed (Fig. 7d). That is, the pressure measured at Sensor 1 in the uncoupled simulations is always higher than that in the coupled FSI approach. It is important to emphasize that Sensor 1 is located 24.5 cm upstream of the test specimen (see Fig. 1a) and that the peak pressure immediately after reflection is assumed to be independent of the stiffness of the structure (see, e.g., [25]). The observed FSI effects at Sensor 1 are summarized in Table 2, providing the peak reflected overpressure $p_{r,max}$ and the saturated impulse $i_{r+,sat}$ for the coupled and the uncoupled approach. The saturated impulse $i_{r+,sat}$ is found by using the pressure history at Sensor 1. The integral of the reflected overpressure is taken from the time of arrival of the reflected pressure at Sensor 1 (see second jump in pressure in Fig. 7d) over the time interval $t_{d+,sat}$, which corresponds to the time interval of the dynamic response before the plate reaches its permanent deformation. The same trend is observed for the loading as for the mid-point deflections, i.e., both the peak reflected overpressure and the saturated impulse are reduced in the coupled simulations. Moreover, higher blast pressure magnitudes result in increased FSI effects.

Fig. 7c-d also show that the incident (side-on) pressures were in excellent agreement, indicating that the reduced reflected overpressure may be due to the deformation of the plates. This was also observed in previous studies, which indicated that the blast mitigation could be related to the induced velocity in the plate (see, e.g., [23–25]), while Hanssen et al. [26] suggested that the reduction in reflected pressure is due to the deformed shape of the plate which resembles a global dome. Hanssen et al. [26] argued that the deformed shape produces a non-uniform spatial and temporal distribution of the pressure in the vicinity of the plate. The reduction in reflected pressure seems to occur over a period in time that is similar to the saturated durations $t_{d+,sat}$ listed in Table 3. Then, very limited FSI effects are observed throughout the remaining part of the positive phase (Fig. 7c). This makes it natural to relate the reduction in reflected pressure to the induced velocity in the plate.

Fig. 8 shows a comparison of the plate deformation profiles in an attempt to investigate the influence of FSI effects on the deformed shape of the plates. The deformation profiles are extracted at magnitudes of 0 %, 25 %, 50 %, 75 % and 100 % of maximum mid-point deflection in both the uncoupled and coupled simulation. The comparison is limited to test D35, since the same trend was observed in all tests.

As expected, the deformation profiles show a similar trend to the mid-point deflections as in Fig. 7a. That is, the uncoupled approach predicts larger deformations than the corresponding fully coupled FSI simulations. The trend is that higher deformation magnitudes result in increased FSI effects during the dynamic response of the plates. It is also noted that the deformation profiles in the two approaches have more or less the same shape at the same level of deflection, but with different magnitudes. Both approaches show the characteristic behaviour of blast-loaded plates, where plastic yield lines are first formed near the support and then travel towards the centre of the plate (see, e.g., [49]). This in-

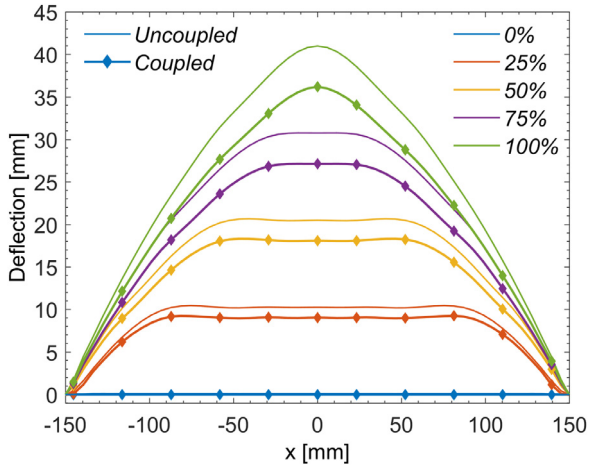

Fig. 8. Comparison of deformation profiles at 0 %, 25 %, 50 %, 75 % and 100 % of maximum deflection for the uncoupled and coupled approach in test D35. The deformation profiles are extracted from the centre along the x-axis.

dicates that the mid-point velocities in Fig. 7b may be a good estimate of the induced velocity in the plate during the FSI. Thus, the mid-point velocities are representative for the straight, horizontal part of the plate located in-between the plastic yield lines until they meet at the centre. This builds confidence in the fact that the induced velocity in the plate produces the observed pressure drop in front of the plate (Fig. 7c-d), which is also in accordance with studies on FSI effects during the response of free-standing plates (see, e.g., [23–25]).

Fig. 9 contains a comparison of the predicted overpressure in the vicinity of the plate in the uncoupled and the coupled FSI approach. The comparison is carried out at characteristic times in test D35 and shows the pressure acting on the loaded surface of the plate and the full view of a longitudinal cross-section in the center of the tube. This view of the cross-section is obtained by mirroring the quarter-model across one symmetry plane, and this view is only used for visualization purposes of the pressure distribution near the F-S interface. Note that the tank was not present in the uncoupled approach (see Fig. 3b); however, the 'virtual' contour of the tank is included in the uncoupled contour maps as a grey shaded line to indicate the corresponding fluid volume surrounding the plate in the coupled simulation.

As expected from a rigid reflecting surface, the uncoupled simulation shows planar, uniform wave fronts throughout the entire simulation (left part of Fig. 9a–f). A planar, uniform pressure wave is also observed in the coupled simulation immediately after the initial reflection when the reflected shock wave starts travelling from right to left (right part of Fig. 9a). Then, as the plate starts moving in the coupled simulations, the deformation of the steel plate induces a non-uniform spatial and temporal distribution of the pressure near the plate (Fig. 9b–e). This is first observed as a reduced pressure in the central part of the plate (Fig. 9b), resulting in pressure waves that propagate both radially and to the left (Fig. 9c–e). As the plate deforms, it undertakes a curved shape that seems to result in a focusing effect of the pressure in the central part of the plate (Fig. 9d–e). There is a trend of a reduction in reflected pressure before the maximum deformation is reached at approximately $t = 1.14$ ms (Fig. 9b–c). Then, an increase in maximum pressure is observed in Fig. 9d at $t = 1.20$ ms. The radial pressure waves continue until the end of the elastic rebound (Fig. 9e) when the plate reaches its permanent deformation. Thereafter, only limited FSI effects are observed throughout the remaining part of the simulation (see Fig. 9f).

This makes it natural to relate the reduction of mid-point deflection in Fig. 7a to both the deformed shape and the induced velocity in the plate, which alters the reflected pressure in the vicinity of the plate. That is, the initial reduction in reflected pressure is related to the induced velocity of the plate (right part in Fig. 9b), while the subsequent increase in peak reflected pressure may be due to the deformed shape of the plate that induces a non-uniform pressure distribution (pressure focusing effect) in the centre of the plate (see right part in Fig. 9d). It is interesting to note that the increase in pressure magnitude at maximum deflection in the fully coupled approach (right part of Fig. 9d) is larger than that in the uncoupled approach (left part of Fig. 9d).

The trend shown for test D35 in Fig. 9 is representative of all tests under consideration in this study. That is, the effect of the induced velocity in the plate tends to reduce the pressure, while the deformed shape of the plate induces pressure magnitudes larger than those in the Eulerian simulations (pressure focusing effect). It is interesting to note that the increase in pressure magnitudes occurs more or less at the instant of maximum deformation in the plate. To the authors' best knowledge, there are no previous studies on clamped steel plates that observe this type of FSI effect in terms of increased pressure due to the deformed shape of the plate (Fig. 9d).

3.5. Interpretation of the FSI effects

This interpretation of the pressure waves occurring during the FSI part of the dynamic response is corroborated in Fig. 10 by a more detailed investigation of the resulting wave patterns. Fig. 10 shows the density gradient to visualize the variations in the resulting wave pattern close to the plate. This type of visualization is similar to the Schlieren technique that is often used in experiments to represent small differences in pressure, i.e., the location and magnitude of expansion and compression regions in a fluid flow (see, e.g., [50]). The uncoupled and the coupled FSI approach are shown in the left and right column, respectively, of the figure for each instant of interest. Note that the chosen times of interest are similar to those in Fig. 9 except that t = 1.90 ms is replaced by t = 0.80 ms to obtain more insight into the wave patterns during the initial phase of the plate response. To obtain a reasonable resolution of the density gradient, it was necessary to use an even finer mesh than that in the remaining parts of this study. The fluid mesh was therefore refined even further by using two additional levels of FSI-driven AMR in the fluid sub-domain. This resulted in a mesh size of 1.25 mm in the fluid surrounding the plate (see Fig. 10a). Note that the additional refinement was useful to improve flow visualization, but it had no visible effects on the results presented so far concerning the plate deformation and the pressure time histories.

The reflected shock wave can be seen as the planar wave with a distinct density gradient propagating from right to left. As expected, it is observed that the shock wave reflects on a planar surface in both the uncoupled and coupled simulation (Fig. 10a). Thus, the planar nature of the shock wave is not altered during or after the reflection itself. However, as soon as the plate starts to undergo deformations, it is evident that the FSI introduces a significantly more complex wave pattern in the region behind the reflected shock wave (see Fig. 10b–f). This is particularly evident when comparing these observations to those in the uncoupled simulation, where the shock wave reflects on a non-deformable surface. The FSI generates a series of compression and expansion waves propagating both in the longitudinal and in the transversal direction of the tube. Eventually, the transversal waves meet in the centre, resulting in a focusing of the compression waves at the plate centre (see Fig. 10e), which then results in the increase and focusing of the pressure as observed in Fig. 9d. It is interesting to note that this point in time corresponds to the elastic rebound of the plate, immediately after the time of peak deflection ($t = 1.14$ ms).

Then, as the plate reaches its permanent deformed configuration at $t = 1.25$ ms, it is observed that some small disturbances are generated behind the plate as the plate undergoes elastic oscillations around the permanent deflection (see Fig. 10e–f). These small disturbances seem to initiate during the elastic rebound of the plate (see Fig. 10e) and then propagate along the plate surface as a result of conservation of momentum in the air (see Fig. 10f). However, despite the relatively strong density gradient of these disturbances, this last phase of the FSI has limited

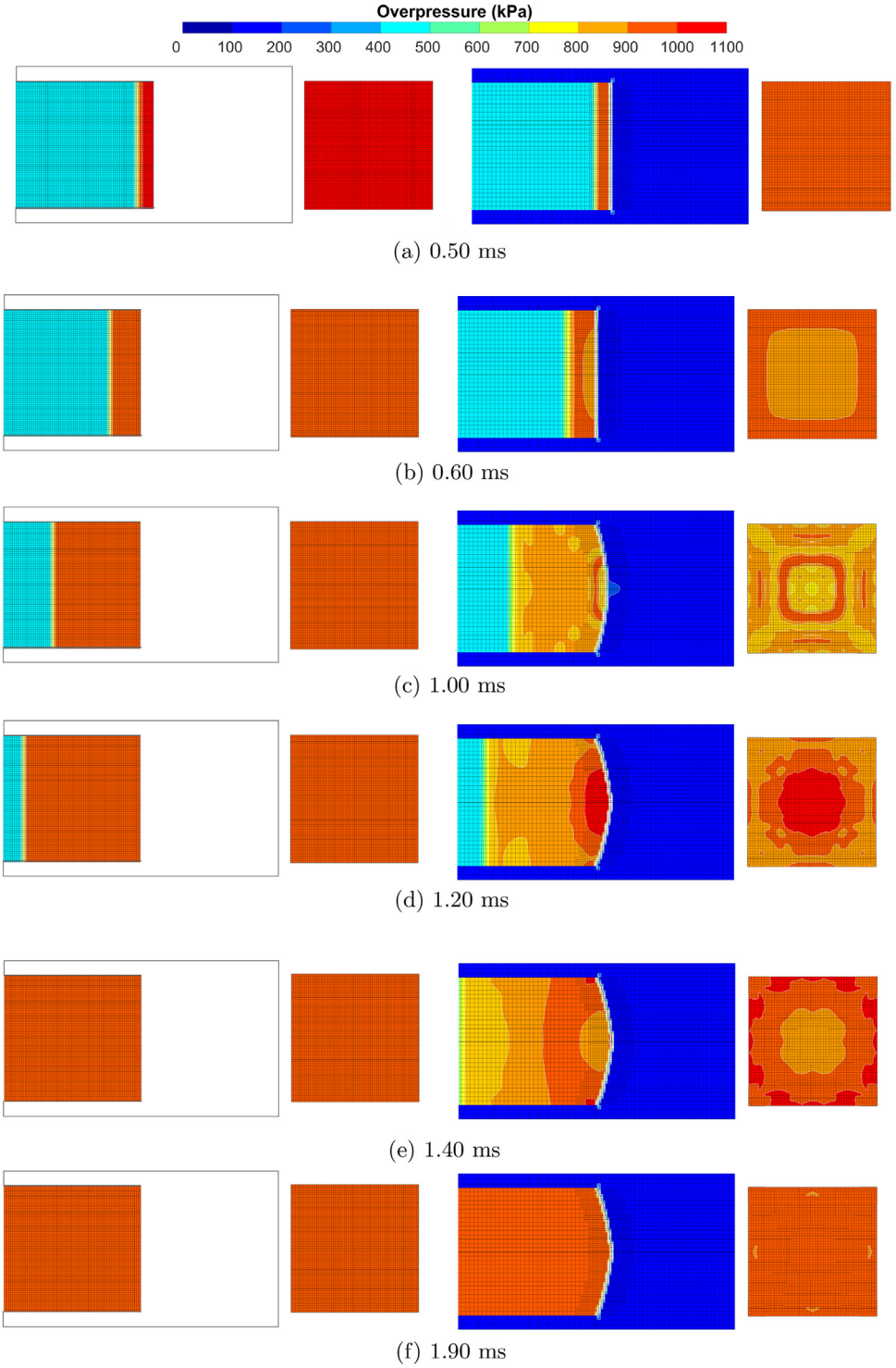

Fig. 9. Comparison of the uncoupled (left) and coupled (right) FSI approach at characteristic times in test D35. Fringe colours represent the contour map of the overpressure (in kPa) in the vicinity and on the plate. Cross-sectional views along the centre of the fluid are shown to enable a clear view of the fluid-structure interface. Time zero ($t = 0$) is taken as the arrival of the shock wave at Sensor 1 located upstream of the test specimen (see Fig. 1a).

influence on the pressure field downstream of the plate (see right side of plate in Fig. 9d–e).

It should also be noted that a strong gradient is observed (dark blue zone) over the thickness of the plate in all of the coupled simulations. This zone of high gradient coincides with the influence domain of the *FLSW* algorithm (see Fig. 2) and represents the sudden change in pressure and density across the plate.

The detailed investigation of the density gradient in Fig. 10 confirms that the pressure waves in front of the plate are due to the induced motion and deformed shape of the plate. A series of planar compression and expansion waves initiate from the central part of the plate (see Fig. 10b–d), where plastic yield lines form a planar area that reduces in size as the yield lines propagate towards the plate centre (Fig. 8). These pressure waves result in a pressure drop in front of the plate (Fig. 9a–c). At the same time, radial waves initiate at the location of the yield lines surrounding this planar area. Eventually, these radial waves meet at the plate centre (see Fig. 10e), producing a focusing effect that corresponds to the pressure increase in Fig. 9d.

Fig. 11 illustrates additional results on the exposed plate area (Fig. 11a) and the approach used to obtain the pressures acting on the

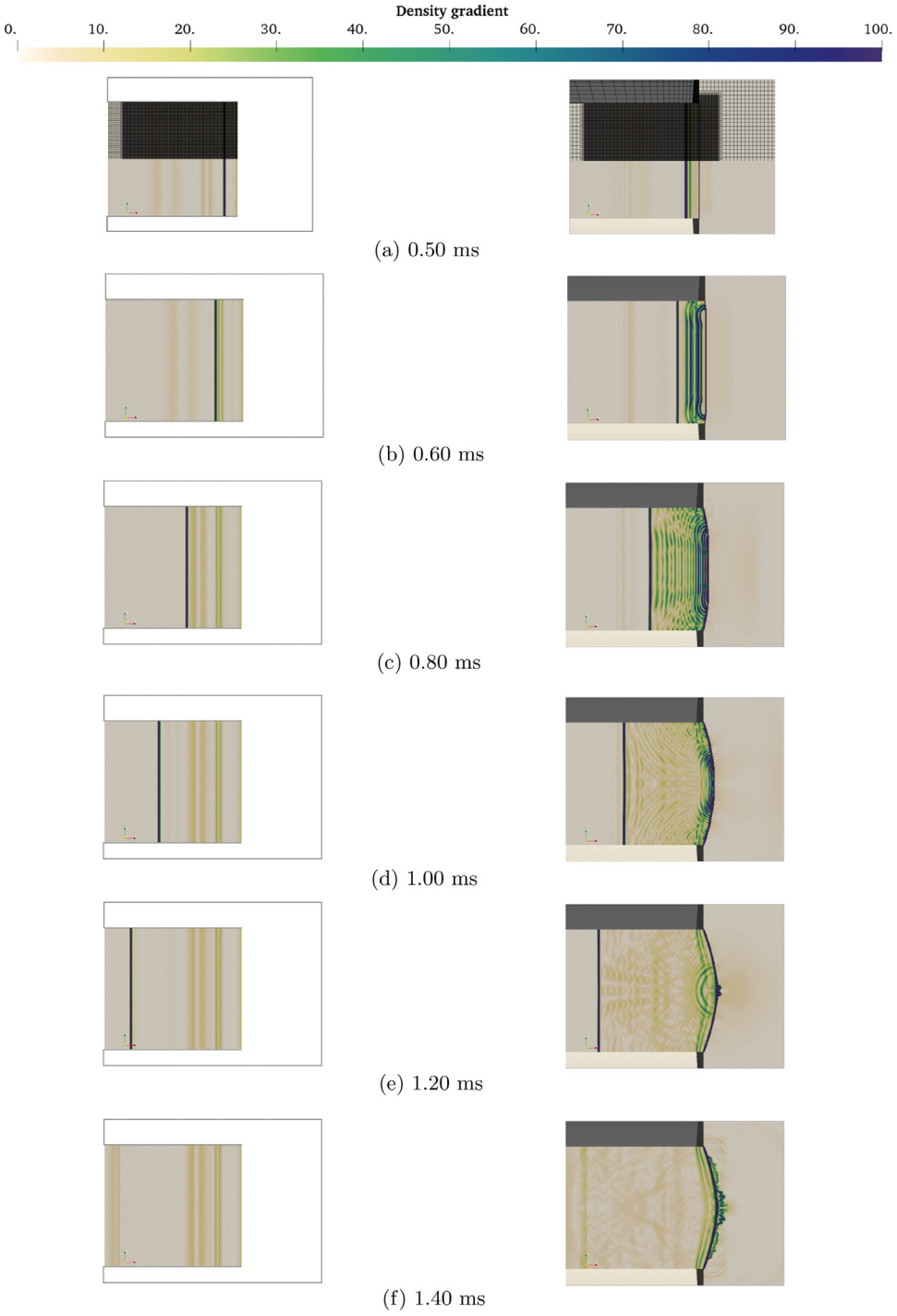

Fig. 10. Visualization of pressure waves generated during the uncoupled (left) and coupled (right) FSI approach at characteristic times in test D35. Fringe colours represent the contour map of the density gradient magnitude. The fully refined fluid mesh is also shown on one quarter of the model in (a). Sensor 1 is located at the roof of the tube and at the position of the left vertical edge of each image.

plate (Fig. 11b) in conjunction with the embedded (*FLSW*) FSI technique. The pressure acting on the plate is obtained using the *EFSI* functionality in EPX. This basically extracts the fluid pressure in the closest meaningful fluid element, i.e., by disregarding elements within the structural influence domain (see Fig. 2). Fig. 11b gives a close-up of the F-S interface in the right part of Fig. 9d, where the plate is illustrated as a thick black line. The width of the structural influence domain is indicated by D and is in the order of two fluid elements (at the maximum refinement level of the FSI-driven AMR). The fluid pressure on the blast-exposed area of the plate is extracted from the surface labelled as 'EFSI plate' and represented by a thick dotted line in Fig. 11b. This *EFSI* surface is located at a certain distance d from the actual position of the plate because the numerical fluxes are blocked at all CCFV interfaces within the structural influence domain (see also Fig. 2). This implies that the pressure and other physical quantities in the fluid elements located inside the influence domain, are not meaningful physically and thus not representative of the actual pressure acting on the plate. Note the smeared pressure gradient across the plate in Fig. 11b, observed as a gradual change in fringe values from yellow to blue across the plate. This also illustrates the interest of using FSI-driven AMR in order to reduce the size of the influence domain and of increasing the accuracy of the embedded FSI algorithm to obtain more precise pressure distributions on the plate.

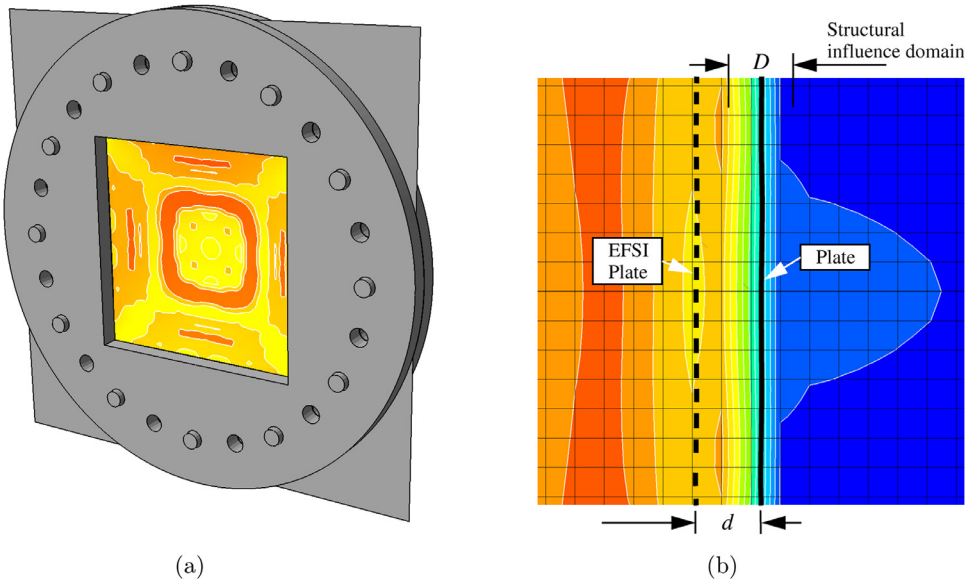

Fig. 11. Illustration of the pressure loading in the vicinity of the plate in test D35 at $t = 1.00$ ms: (a) cross-sectional view of surface overpressure acting on the exposed area of the plate (same as in Fig. 9c), and (b) close-up on the influence domain in the cross-sectional view. Fringe colours represent the contour map of the overpressure (in kPa) in the vicinity of the plate, where the colourbar is the same as in Fig. 9.

4. Experimental validation

As already stated in Section 3.3, the studies on FSI effects were conducted by purely numerical investigations in this work. That is, no results from the experimental campaign were used in preparing or calibrating the numerical simulations. The chosen computational strategy ensured that the incoming blast wave was perfectly identical in both the uncoupled and coupled approach, to enable both qualitative and quantitative studies, within the limitations of the numerical model, on the influence of FSI effects on the dynamic response of blast-loaded steel plates. However, from an engineering point of view, comparison with experimental data is always of interest to evaluate the predictive capabilities of the numerical methodology in capturing the actual physics of the problem. The results from the fully coupled simulations are therefore compared to the corresponding results obtained from the experiments presented in Section 2. The experimental validation was focused on three performance indicators in terms of the structural response, i.e., the mid-point deflections, the mid-point velocities and the deformation profiles. In addition, the pressure measurements at Sensor 1 were used to assess the performance of the fluid sub-domain in predicting the blast loading.

Fig. 12a-b compare the mid-point deflections and mid-point velocities in the plate, respectively, for the coupled approach to those in the experiments, while Fig. 12c-d contain the corresponding pressure histories at Sensor 1. It should be noted that Fig. 12d contains the same data as Fig. 12c, but with a closer view on the initial pressure measurements at Sensor 1. The main purpose of Fig. 12d is therefore to compare the numerical predictions of the fully coupled approach with the corresponding measurements in the experiments in terms of incoming and reflected overpressures. Fig. 13 compares the deformation profiles at magnitudes of 0 %, 25 %, 50 %, 75 % and 100 % of maximum mid-point deflection in both the coupled simulation and the experiment. As in Fig. 8, the comparison is limited to test D35 since the same trend was observed in all tests. It should be noted that such comparisons of deformation profiles should be carried out with caution. Due to the discrete nature (i.e., temporal discretization) of the data sampling in both the numerical solutions and in the experiments, it can be difficult to compare the profiles at the exact same magnitude of deformation. The fast dynamic nature from 0 % to 100 % of maximum mid-point deflection, which typically takes place in less than 1 ms, makes the extracted deformation profiles quite sensitive to the exact time instant chosen for visualization. Despite this inherent sensitivity of these comparisons, the comparison of deformation profiles is valuable in evaluating the predictive capabilities of the numerical model. To reduce the inherent error in the comparison because the sampling instants in the experiments do not exactly coincide with those in the simulations, the simulated profiles are linearly interpolated between the two nearest sampling instants.

The fully coupled simulations were generally in good agreement with the experimental data. Excellent agreement is obtained with respect to mid-point deflections (Fig. 12a) and mid-point velocities (Fig. 12b) for tests D05 to D35, while the simulation of test D60 seems to slightly underestimate the deflections and velocities. The deformation profiles are also in very good agreement with the experimental observations (see Fig. 13). A larger discrepancy between computed and experimental profiles is observed for the lowest values of deflection (0% and 25%), which is as expected given the difficulty of measuring such small values under highly dynamic conditions. A comparison of the pressure histories at Sensor 1 shows an excellent agreement in the time of arrival of the reflected shock wave, indicating that the velocity of that wave is well captured by the numerical model. Minor deviations were observed in the pressure magnitudes (see Fig. 12d). These deviations were observed, except for the lowest pressure magnitude, in both the incoming and the reflected overpressure. The incoming pressures and the first part of the reflected overpressure were slightly underestimated, while the reflected overpressure tends to be slightly overestimated throughout the remaining part of the pressure histories (Fig. 12d). It is however challenging to conclude on the influence of these minor deviations regarding the dynamic response of the thin steel plates. This is because Sensor 1 is located upstream of the test specimen (see Fig. 1a), since it would be difficult to mount pressure sensors on the thin plate without altering its structural characteristics. Thus, Sensor 1 does not measure the pressure on the steel plates but rather the pressure in the roof of the shock tube and 24.5 cm upstream of the thin steel plates.

Since these are minor deviations if one considers the sophistication of the numerical methodology necessary to accurately predict the pressure waves occurring in these types of shock tube tests, it can be concluded that the overall performance of the fluid sub-domain is acceptable. It is important to emphasize that there is considerable complexity in these simulations, where one of the main challenges is to model the diaphragm failure process and its influence on the resulting wave patterns inside the shock tube. Further improvements of the numerical accuracy in predicting the blast wave formation in the SSTF will need to focus even more on the modelling of the diaphragm failure process (see Fig. 5). This aspect has already been identified in a recent study by the authors [51],

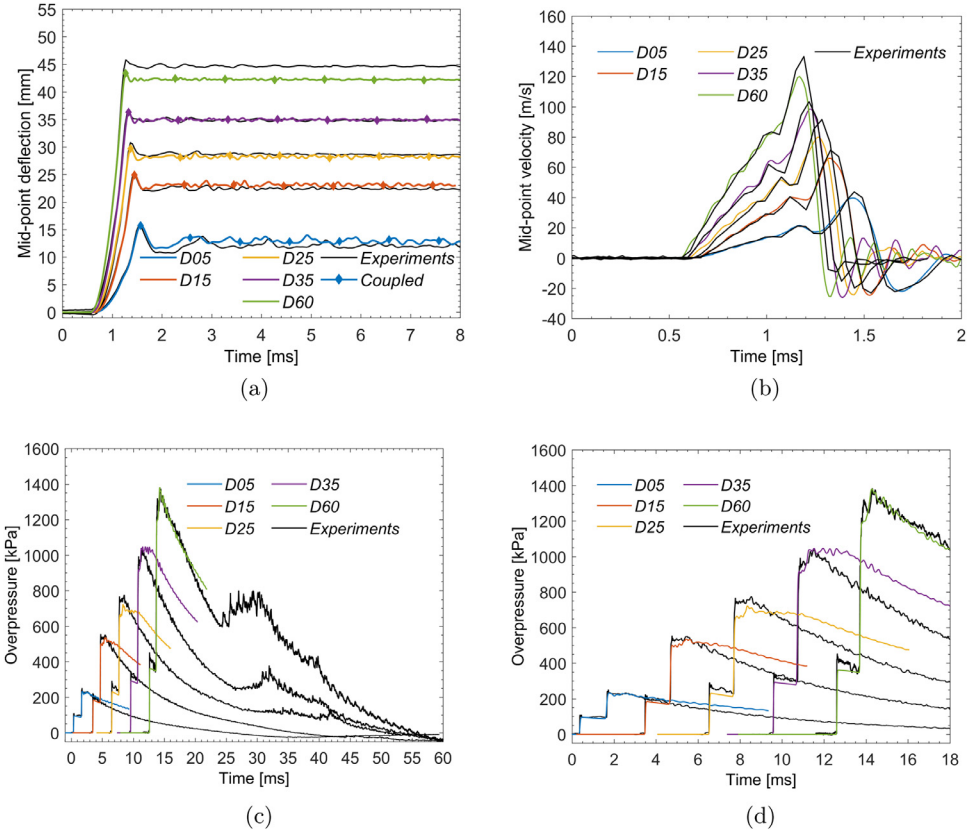

Fig. 12. Comparison of experimental measurements and corresponding numerical predictions in the fully coupled simulations: (a) Mid-point deflections, (b) mid-point velocities, (c) pressures measured at Sensor 1 and (d) the same data as Fig. 12c where the time axis is more focused on the reflected overpressure. Note that the curves in Fig. 12c-d are shifted in time for improved readability. Each curve was right-shifted 3 ms with respect to the previous one.

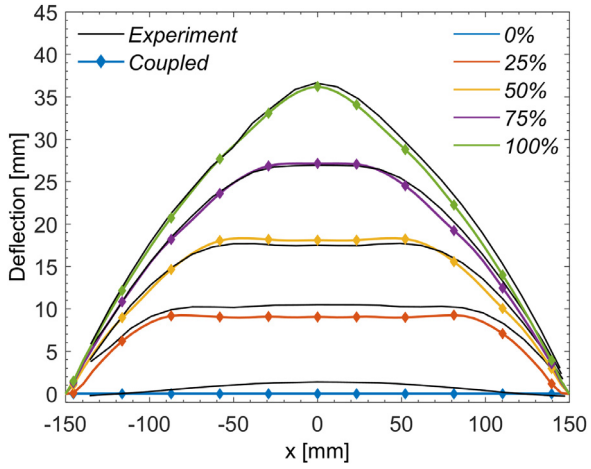

Fig. 13. Deformation profiles at 0 %, 25 %, 50 %, 75 % and 100 % of maximum deflection for the coupled approach and experimental data in test D35. The deformation profiles are extracted from the centre along the x-axis.

but it is left as further work since the level of accuracy already reached is sufficient to evaluate FSI effects. Detailed investigations of the diaphragm failure process can therefore be considered beyond the scope of the present study. This study focuses on the FSI effects during the dynamic response of the plates using a purely numerical approach. Experimental validation is only used to evaluate the predictive capabilities of the numerical methodology. The already very good agreement with experimental observations in Figs. 12 and 13 provides confidence in the use of the present numerical model and in the fact that the numerical studies on FSI can be carried out numerically, both in a qualitative and quantitative manner. Hence, the numerical methodology presented herein can be used to obtain more insight into the underlying physics observed in the experiments.

5. Concluding remarks

The present study investigates FSI effects during the dynamic response of blast-loaded steel plates. Such effects were studied by comparing the numerical predictions of the uncoupled and coupled FSI approach. Purely Eulerian simulations were used to generate the loading in the uncoupled approach. Special focus was placed on the influence of FSI on the mid-point deflections and mid-point velocities in the plates, where experimental data served as a backdrop to evaluate the accuracy of the numerical simulations. The main conclusions from the study are as follows.

- Fluid-structure interaction (FSI) takes place if the steel plate moves or deforms during the duration of the blast load.
- The influence of FSI effects is quantified in terms of the deflections, the pressures and the saturated impulse. As expected, the uncoupled approach provides conservative predictions for the dynamic response in the plates, i.e., it overestimates the plate deflection, due to the inherent assumption that the pressure is unaltered by the plate deformation. The clear trend is that higher blast pressure magnitudes result in increased FSI effects in the fully coupled simulations, resulting in reduced deflections and velocities in the plate. It was observed that the mid-point deflections were reduced by 4–14 %, depending on the blast intensity, when considering FSI.
- Fully coupled simulations showed that the dynamic response of the steel plate introduces a non-uniform spatial and temporal distribution of the pressure near the plate. The fact that the induced velocity in the plate tends to reduce the pressure was confirmed, in accordance with previous studies in the literature. However, the observed successive increase in pressure due to the deformed shape of the plate was unexpected. It was interesting to note that the pressure

magnitudes in the fully coupled FSI simulations were (for a short period) larger than those in the Eulerian simulations. This increase in pressure occurred more or less at the same time as the elastic rebound of the plate, immediately after reaching the maximum deformation in the plate. To the authors' best knowledge, there are no previous studies on clamped steel plates reporting this type of FSI effect in terms of increased pressure due to the deformed shape of the plate. Neglecting FSI effects may then result in a non-conservative estimate of the loading. Although the uncoupled approach gave conservative predictions for the deformation of the steel plates considered in this study, the focusing effect may be of more importance for other types of flexible and lightweight structures if the increase in pressure occurs before the permanently deformed configuration. The important observation in this study was that the non-uniform pressure distribution in front of the plate was due to a combination of both the induced velocity and deformed shape of the plate.

- The numerical predictions showed very good agreement with the experimental observations. The coupled FSI simulations were able to predict both the dynamic response of the plate and the pressure distribution in front of the plate with good accuracy. The clear conclusion from this study is that the uncoupled approach can be used for smaller blast intensities on clamped thin steel plates, but it provides conservative predictions for larger blast intensities. That is, fully coupled FSI simulations are necessary to obtain both qualitative and quantitative predictions at higher pressure magnitudes of the blast loading.
- The qualitatively and quantitatively good agreement presented in this study was obtained as a result of extensive use of advanced numerical simulation techniques, of which the most important were found to be the embedded FSI model (*FLSW*), the automatic AMR in the fluid (to increase FSI accuracy) and in the diaphragms (to accurately model their failure) and a realistic modelling of the mechanical boundary conditions for the plate (allowing for in-plane sliding of the plate with respect to the clamping frames). The modelling of the diaphragm failure process was confirmed to be a critical point in order to obtain a realistic blast loading on the plate. Many complex phenomena are involved in the diaphragm failure process and, although the present results are already satisfactory, further refinement and improvement of the diaphragm modelling may be required in future investigations. However, this is beyond the scope of this study and will be addressed in future works.
- The experimental and numerical methodologies presented herein can be used to obtain more insight into the underlying physics during the dynamic response of clamped thin steel plates exposed to blast loading. This motivates further studies on FSI effects during the dynamic response of other civil engineering structures to identify scenarios where FSI may be of importance in blast-resistant designs. This study indicates that, as long as the structure does not fail, FSI effects could mitigate the blast loading acting on a lightweight and flexible structure. That is, lightweight structures undertake less momentum compared to heavier structures when exposed to the same blast intensity since a lightweight structure experiences a larger induced velocity, which, in turn, reduces the pressure acting on the structure.

Declaration of Competing Interest

The authors declare that they have no known competing financial interests or personal relationships that could have appeared to influence the work reported in this paper.

CRediT authorship contribution statement

Vegard Aune: Conceptualization, Data curation, Formal analysis, Writing - original draft. **Georgios Valsamos:** Conceptualization, Data curation, Formal analysis, Writing - original draft. **Folco Casadei:** Conceptualization, Data curation, Formal analysis, Writing - original draft. **Magnus Langseth:** Conceptualization, Writing - review & editing. **Tore Børvik:** Conceptualization, Formal analysis, Writing - original draft.

Acknowledgements

This work has been carried out with financial support from NTNU and the Research Council of Norway through the Centre for Advanced Structural Analysis (CASA), Centre for Research-based Innovation (Project No. 237885). The financial support by the Norwegian Ministry of Justice and Public Security is also greatly appreciated.

Appendix A

A1. Governing equations

Structures are characterized by well-defined shapes, which makes a material framework suitable to express their motion since each individual node of the computational mesh follows the associated material particle. The computations in the structural sub-domain are therefore performed using a Lagrangian formulation, where EPX solves the conservation of momentum, also known as the dynamic equilibrium, arising from the principal of virtual power

$$\int_V \delta\mathbf{v}^{\mathrm{T}}\rho\frac{\partial\mathbf{v}}{\partial t}\mathrm{d}V + \int_V \mathrm{tr}((\nabla\delta\mathbf{v})^{\mathrm{T}}\cdot\boldsymbol{\sigma})\mathrm{d}V - \int_V \delta\mathbf{v}^{\mathrm{T}}\rho\mathbf{f}_{\mathrm{b}}\mathrm{d}V - \int_S \delta\mathbf{v}^{\mathrm{T}}\mathbf{t}\mathrm{d}S = 0 \tag{1}$$

where ρ is the mass density of the current volume V with boundary surface S, $\mathbf{v}$ and $\delta\mathbf{v}$ are the vectors of velocities and virtual velocities at any point (x, y, z) within V, respectively, $\boldsymbol{\sigma}$ is the Cauchy (true) stress, $\nabla\delta\mathbf{v}$ is the spatial gradient of the virtual velocity vector, $\mathbf{f}_{\mathrm{b}}$ are the volumetric forces per unit mass and $\mathbf{t}$ are boundary surface tractions. By spatial discretization of the structure (using finite elements) Eq. (1) reads

$$\boldsymbol{M}\boldsymbol{a} = \boldsymbol{F}^{\mathrm{ext}} - \boldsymbol{F}^{\mathrm{int}} \tag{2}$$

where $\boldsymbol{M}$ is the lumped (diagonal) mass matrix, $\boldsymbol{a}$ is the vector of nodal accelerations, $\boldsymbol{F}^{\mathrm{ext}}$ are the external forces and $\boldsymbol{F}^{\mathrm{int}}$ are the internal forces. The forces are found by spatial integration over the elements as

$$\boldsymbol{F}^{\mathrm{ext}} = \sum_{n=1}^{N_{\mathrm{els}}}\int_{S_n}\boldsymbol{N}^{\mathrm{T}}\mathbf{t}\mathrm{d}S + \sum_{n=1}^{N_{\mathrm{els}}}\int_{V_n}\boldsymbol{N}^{\mathrm{T}}\rho\mathbf{f}_{\mathrm{b}}\mathrm{d}V\ , \qquad \boldsymbol{F}^{\mathrm{int}} = \sum_{n=1}^{N_{\mathrm{els}}}\int_{V_n}\boldsymbol{B}^{\mathrm{T}}\boldsymbol{\sigma}\mathrm{d}V \tag{3}$$

where V_n is the volume of the element n, $\boldsymbol{N}$ is the matrix of shape functions, $\boldsymbol{B}$ is the matrix of shape function derivatives, and the summation sign Σ is the assembly operator over all elements from 1 to N_{els}. Eq. (2) is solved explicitly using the lumped mass matrix and is directly integrated in time using the central difference scheme [5,33].

Blast wave propagation is essentially an inviscid compressible flow. The viscosity is assumed to be zero and the fluid can assume any shape but is incapable of developing shear stresses. It is therefore preferable to express the conservation laws for the fluid in a spatial (Eulerian) framework, where the computational mesh is fixed while the fluid (particles) moves relative to these grid points. EPX solves the conservation of mass, momentum and energy in the fluid sub-domain, given in vector form as

$$\frac{\partial\mathbf{U}}{\partial t} + \nabla\cdot\mathbf{F}(\mathbf{U}) = \mathbf{0} \quad \text{with} \quad \begin{cases}\mathbf{U} = [\boldsymbol{\rho} \quad \boldsymbol{\rho}\mathbf{v} \quad \mathbf{E}]^{\mathrm{T}} \\ \mathbf{F} = [\rho\mathbf{v} \quad \rho\mathbf{v}\mathbf{v} + p\mathbf{I} \quad (E+p)\mathbf{v}]^{\mathrm{T}}\end{cases} \tag{4}$$

where $\mathbf{U}$ is the vector of conserved variables, $\mathbf{F}$ is the associated flux matrix, ρ is the density, $\mathbf{v} = v_i\mathbf{e}_i = [v_1\ v_2\ v_3]^{\mathrm{T}}$ is the fluid (particle) velocity vector with components v_1, v_2 and v_3 along each of the basis vectors $\mathbf{e}_i$ in a Cartesian coordinate system, $E = \rho(e + \frac{1}{2}\mathbf{v}^{\mathrm{T}}\mathbf{v})$ is the total energy per unit volume, e is the specific internal energy per unit mass (given by a suitable equation of state), $\frac{1}{2}\mathbf{v}^{\mathrm{T}}\mathbf{v}$ is the kinetic energy per unit mass, p is the pressure and ∇ is the spatial gradient operator.

Table A.1
Material parameters and physical constants [36] for the dual-phase steel used in the shock tube tests in Section 2.

Material properties								Physical constants						
A	Q_1	C_1	Q_2	C_2	c	m	$\dot{p}_0$	E	ν	ρ	c_p	χ	T_r	T_m
[MPa]	[MPa]	[-]	[MPa]	[-]	[-]	[-]	[s^{-1}]	[GPa]	[-]	[kg/m^3]	[J/kgK]	[-]	[K]	[K]
325.7	234.8	56.2	445.7	4.7	0.01	1.0	5×10^{-4}	210.0	0.33	7850	452	0.9	293	1800

Integrating the local conservative form of the Euler equations in Eq. (4) over a control volume fixed in space reads

$$\frac{\partial}{\partial t}\int_{V_f}\mathbf{U}\mathrm{d}V+\int_{S_f}\mathbf{F}(\mathbf{U})\cdot\mathbf{n}\mathrm{d}S=0 \tag{5}$$

where $\mathbf{n}$ is the outward unit normal to the boundary surface S_f of the fixed control volume V_f, and the Gauss (divergence) theorem is used to find the flux through the boundary surface of the control volume. The physical interpretation of Eq. (5) is that the time variation of $\mathbf{U}$ included in the fixed volume V_f is balanced by the flow of $\mathbf{U}$ through its boundary surface S_f. Using an appropriate discretization in space for the fluid and choosing a suitable discretization of the flux through the boundary surface, the non-linear set of differential equations in Eq. (4) may be solved for the discretized unknowns $\mathbf{U}_i$ located at Gauss points (typically at the element centroid and represented by an average value) [5,33]. Thus, the control volume is viewed as a continuum and equilibrium is characterized by no gradients in the conserved variables $\mathbf{U}$ (velocity, pressure, temperature). That is, the physical properties are uniform over each control volume.

A2. Material models

Eq. (4) contains five conservation equations, i.e., conservation of mass, conservation of momentum in the three spatial dimensions and conservation of energy, and six unknowns. Hence, to find a unique solution of Eq. (4) it is necessary to relate the pressure to the conserved variables by a suitable equation of state (EOS). A commonly used EOS for air is the ideal gas law (called *GAZP* in EPX). This EOS is found in many forms and variations in the literature. However, all these representations are basically the same and this study uses the particular form given by

$$p=\rho(\gamma-1)e \tag{6}$$

where ρ is the density, e is the specific internal energy per unit mass, $\gamma=c_p/c_v$ is the ratio of specific heats given by the specific heat at constant pressure c_p and the specific heat at constant volume c_v. The specific internal energy is given as $e=RT/(\gamma-1)$ for an ideal gas behaviour, where T is the temperature and R is the specific gas constant which is unique for each gas. The initial conditions for each simulation were taken from Table 1.

The non-linear material behaviour of the steel plates was represented using the *VPJC* material model in EPX [44]. This model allows for finite strains and rotations, high strain rates, temperature softening and ductile fracture. The plasticity is governed by the von Mises yield criterion, the associated flow rule and a modified Johnson-Cook relation by using the Voce [52] hardening rule for the flow stress. This results in the following dynamic yield function f_d governing the behaviour of the steel material [53,54]

$$\begin{aligned}f_d(\boldsymbol{\sigma},p,\dot{p},T)&=\sigma_{\mathrm{eq}}(\boldsymbol{\sigma})-\sigma_y(p,T)\left(1+\frac{\dot{p}}{\dot{p}_0}\right)^{\mathrm{c}}\\&=\sqrt{\frac{3}{2}\boldsymbol{\sigma}':\boldsymbol{\sigma}'}-\left(\sigma_0+\sum_{k=1}^{2}Q_k\left[1-\exp(-C_kp)\right]\right)\\&\quad\times\left(1+\frac{\dot{p}}{\dot{p}_0}\right)^{\mathrm{c}}\left(1-T^{*\mathrm{m}}\right)\end{aligned} \tag{7}$$

This yield function is used to update the Cauchy stress $\boldsymbol{\sigma}$ in Eq. (3), where σ_{eq} is the equivalent von Mises stress, σ_y is the flow stress, p is the equivalent plastic strain, $\dot{p}$ is the equivalent plastic-strain rate, $\dot{p}_0$ is a user-defined reference strain rate, σ_0 represents the initial yield stress, (Q_k, C_k, c, m) are material constants and $\boldsymbol{\sigma}'$ is the deviatoric part of the Cauchy stress tensor. The homologous temperature is defined as $T^*=(T-T_r)/(T_m-T_r)$, where T is the absolute temperature, T_r is the ambient temperature and T_m is the melting temperature of the material. Since the structural response from blast events has a very short duration in time, the temperature evolution was modelled assuming adiabatic conditions and calculated based on the plastic dissipation [53]. Thus, Eq. (7) allows for viscoplasticity when $f_d=0$, while $f_d<0$ means elastic behaviour. Material parameters and physical constants for the steel material used in this study were obtained from the test plates in Section 2 by Aune et al. [36] (see Table A.1).

References

[1] Aleyaasin M, Harrigan JJ, Reid SR. Air–blast response of cellular material with a face plate: an analytical-numerical approach. Int J Mech Sci 2015;91:64–70. doi:10.1016/j.ijmecsci.2014.03.027.

[2] Turkyilmazoglu M. Air blast response of compaction foam having a deformable front face panel incorporating fluid structure interactions. Int J Mech Sci 2016;105:340–7. doi:10.1016/j.ijmecsci.2015.11.010.

[3] Ousji H, Belkassem B, Louar MA, Reymen B, Martino J, Lecompte D, et al. Air–blast response of sacrificial cladding using low density foams: experimental and analytical approach. Int J Mech Sci 2017;128–129:459–74. doi:10.1016/j.ijmecsci.2017.05.024.

[4] Bai X, Zhu L, Yu TX. Saturated impulse for fully clamped square plates under blast loading. Int J Mech Sci 2018;146–147:417–31. doi:10.1016/j.ijmecsci.2017.08.047.

[5] Casadei F, Halleux JP, Sala A, Chillé F. Transient fluid-structure interaction algorithms for large industrial applications.. Comput Methods Appl MechEng 2001;190:3081–110. doi:10.1016/S0045-7825(00)00383-2.

[6] Kambouchev N, Noels L, Radovitzky R. Numerical simulation of fluid-structure interaction between air blast waves and free-standing plates. Comput Struct 2007;85(11–14):923–31. doi:10.1016/j.compstruc.2006.11.005.

[7] Børvik T, Hanssen AG, Langseth M, Olovsson L. Response of structures to planar blast loads - a finite element engineering approach.. Comput Struct 2009;87:507–20. doi:10.1016/j.compstruc.2009.02.005.

[8] Teich M, Gebebeken N. Analysis of FSI effects of blast loaded flexible structures. Eng Struct 2011;55:73–9. doi:10.1016/j.engstruct.2011.12.003.

[9] Aune V, Fagerholt E, Hauge KO, Langseth M, Børvik T. Experimental study on the response of thin aluminium and steel plates subjected to airblast loading. Int J Impact Eng 2016;90:106–21. doi:10.1016/j.ijimpeng.2015.11.017.

[10] Taylor GI. The pressure and impulse of submarine explosion waves on plates. In: Batchelor GK, editor. The scientific papers of Sir G I Taylor, Volume III, Cambridge University Press, UK; 1963. p. 287–303.

[11] Deshpande VS, Fleck NA. One-dimensional response of sandwich plates to underwater shock loading. J Mech Phys Solids 2005;53:2347–83. doi:10.1016/j.jmps.2005.06.006.

[12] Hutchinson JW, Xue Z. Metal sandwich plates optimized for pressure impulses. Int J Mech Sci 2005;47:545–69. doi:10.1016/j.ijmecsci.2004.10.012.

[13] Deshpande VS, Heaver A, Fleck NA. An underwater shock simulator. Proc R Soc A 2006;462:1021–41. doi:10.1098/rspa.2005.1604.

[14] Mori LF, Lee SF, Xue ZY, Vaziri A, Queheillalt DT, Dharmasena KP, et al. Deformation and fracture modes of sandwich structures subjected to underwater impulsive loads. J Mech Mater Struct 2007;2(10):1981–2006. doi:10.2140/jomms.2007.2.1981.

[15] Wadley HNG, Dharmasena K, Chen Y, Dudt P, Knight D, Charette R, et al. Compressive response of multilayered pyramidal lattices during underwater shock loading. Int J Impact Eng 2008;35(9):1102–14. doi:10.1016/j.ijimpeng.2007.06.009.

[16] Xue Z, Hutchinson JW. A comparative study of impulse-resistant metal sandwich plates. Int J Impact Eng 2004;30:1283–305. doi:10.1016/j.ijimpeng.2003.08.007.

[17] Tan PJ, Reid SR, Harrigan JJ. Discussion:"The resistance of clamped sandwich beams to shock loading" (Fleck, N. A., and Deshpande, V. S., 2004, ASME J. Appl. Mech., 71, pp. 386-401). J Appl Mech 2005;72:978–9. doi:10.1115/1.2040452.

[18] Kambouchev N. Analysis of blast mitigation strategies exploiting fluid-structure interaction. Massachusetts Institute of Technology; 2007. Phd thesis.

[19] Kambouchev N, Noels L, Radovitzky R. Nonlinear compressibility effects in fluid-structure interaction and their implications on the air-blast loading of structures. J Appl Phys 2006;100:63519.
[20] Kambouchev N, Radovitzky R, Noels L. Fluid-structure interaction effects in the dynamic response of free-standing plates to uniform shock loading. J Appl Mech 2007;74(5):1042–5. doi:10.1115/1.2712230.
[21] Vaziri A, Hutchinson JW. Metal sandwich plates subjected to intense air shocks. Int J Solids Struct 2007;44:2021–35. doi:10.1016/j.ijsolstr.2006.08.038.
[22] Hutchinson JW. Energy and momentum transfer in air shocks. J Appl Mech 2009;76:51307. doi:10.1115/1.3129773.
[23] Courant R, Friedrichs KO. Supersonic flow and shock waves. New York: Springer-Verlag; 1976.
[24] Toro EF. Riemann solvers and numerical methods for fluid dynamics. 3rd ed. Springer-Verlag Berlin Heidelberg; 2009.
[25] Subramaniam KV, Nian W, Andreopoulos Y. Blast response of an elastic structure: evaluation of the fluid-structure interaction effects. Int J Impact Eng 2009;36:965–74. doi:10.1016/j.ijimpeng.2009.01.001.
[26] Hanssen AG, Enstock L, Langseth M. Close-range blast loading of aluminium foam panels. Int J Impact Eng 2002;27:593–618. doi:10.1016/S0734-743X(01)00155-5.
[27] Gauch HL, Montomoli F, Tagarielli VL. On the role of fluid-structure interaction on structural loading by pressure waves in air. J Appl Mech 2018;85:111007. doi:10.1115/1.4040948.
[28] Yuan Y. Blast response of structures: limits to deformation and fluid-structure interactions. University College London; 2015. Phd thesis.
[29] Yuan Y, Tan PJ, Shojaei KA, Wrobel P. On momentum transfer and external work done to clamped elasto-plastic beams in an air blast. Int J Mech Sci 2018;146–147:377–85. doi:10.1016/j.ijmecsci.2018.07.045.
[30] Menkes SB, Opat HJ. Broken beams - tearing and shear failures in explosively loaded clamped beams. Expe Mech 1973;13:480–6.
[31] Nurick GN, Shave GC. The deformation and tearing of thin square plates subjected to impulsive loads - an experimental study. Int J Impact Eng 1996;18:99–116. doi:10.1016/0734-743X(95)00018-2.
[32] Benson DJ. Chapter 25 - explicit finite element methods for large deformation problems in solid mechanics. Encyclopedia of computational mechanics, 2: Solids. John Wiley & Sons; 2007.
[33] Casadei F, Leconte N. Coupling finite elements and finite volumes by lagrange multipliers for explicit dynamic fluid-structure interaction. Int J Numer MethodsEng 2011;86(1):1–17. doi:10.1002/nme.3042.
[34] Casadei F, Larcher M, Leconte N. Strong and weak forms of a fully non-conforming FSI algorithm in fast transient dynamics for blast loading of structures. In: Proceedings of the 3rd international conference on computational methods in structural dynamics and earthquake engineering (COMPDYN 2011); 2011. p. 1120–39.
[35] Casadei F, Diez P, Verdugo F. An algorithm for mesh refinement and unrefinement in fast transient dynamics. Int J Comput Methods 2013;10:1–31. doi:10.1142/S0219876213500187.
[36] Aune V, Valsamos G, Casadei F, Langseth M, Børvik T. On the dynamic response of blast-loaded steel plates with and without pre-formed holes. Int J Impact Eng 2017;108:27–46. doi:10.1016/j.ijimpeng.2017.04.001.
[37] Roland O, Casadei F, Mouton S, Sobry JF. Propeller blade debris kinematics: blade debris trajectory computation with aerodynamic effect using new FSI formulations. CEAS Aeronaut J 2018;9:683–94. doi:10.1007/s13272-018-0313-4.
[38] Faucher V, Casadei F, Valsamos G, Larcher M. High resolution adaptive framework for fast transient fluid-structure interaction with interfaces and structural failure – application to failing tanks under impact. Int J Impact Eng 2019;127:62–85. doi:10.1016/j.ijimpeng.2018.10.008.
[39] Aune V, Fagerholt E, Langseth M, Børvik T. A shock tube facility to generate blast loading on structures. Int J Protective Struct 2016;7:340–66. doi:10.1016/j.ijimpeng.2016.08.010.
[40] Aune V, Valsamos G, Casadei F, Larcher M, Langseth M, Børvik T. Use of damage-based mesh adaptivity to predict ductile failure in blast-loaded aluminium plates. Procedia Eng 2017;197:3–12. doi:10.1016/j.proeng.2017.08.076.
[41] Aune V. Behaviour and modelling of flexible structures subjected to blast loading. Norwegian University of Science and Technology, Norway; 2017. Ph.D. thesis.
[42] Tasissa AF, Hautefeuille M, Fitek JH, Radovitzky R. On the formation of Friedlander waves on a compressed-gas-driven shock tube. Proc R Soc A 2016;472:20150611. doi:10.1098/rspa.2015.0611.
[43] eCorr. User's manual - eCorr Digital Image Correlation 4.0 Documentation. https://www.ntnu.edu/kt/ecorr [accessed 03.04.2020]; 2020.
[44] EUROPLEXUS. User's manual - a computer program for the finite element simulation of fluid-structure systems under transient dynamic loading; 2020. http://europlexus.jrc.ec.europa.eu [accessed 10.02.2020]
[45] Cast3M. Cast3M software:; 2020. http://www-cast3m.cea.fr/[accessed 03.04.2020]
[46] Paraview. ParaView software:; 2020. https://www.paraview.org/[accessed 03.04.2020]
[47] Andreotti R, Colombo M, Guardone A, Martinelli P, Riganti G, Di Prisco M. Performance of a shock tube facility for impact response of structures. Int J Non-Linear Mech 2015;72:53–66.
[48] Baker W, Cox P, Westine P, Kulesz J, Strehlow R. Explosion hazards and evaluation. Amsterdam: Elsevier; 1983.
[49] Jones N. Structural impact. 2nd ed. Cambridge University Press; 2012.
[50] Smith AJ, Lim TT. Flow visualization: techniques and examples. 2nd ed. Imperial College Press; 2012.
[51] Aune V, Casadei F, Valsamos G, Langseth M, Børvik T. A shock tube used to study the dynamic response of blast-loaded plates. MDPI Proceedings 2018;2:503. doi:10.3390/ICEM18-05395.
[52] Voce E. The relationship between stress and strain for homogenous deformation. J Inst Metals 1948;74:536–62.
[53] Aune V, Valsamos G, Casadei F, Larcher M, Langseth M, Børvik T. Numerical study on the structural response of blast-loaded thin aluminium and steel plates. International Journal of Impact Engineering 2017;99. doi:10.1016/j.ijimpeng.2016.08.010. 131–121
[54] Børvik T, Hopperstad OS, Berstad T, Langseth M. A computational model of viscoplasticity and ductile damage for impact and penetration. Eur J Mech A/Solids 2001;20:685–712. doi:10.1016/S0997-7538(01)01157-3.